Vortex-induced vibration of two circular cylinders in a side-by-side arrangement at moderate Reynolds number_ A numerical study

by Kylie Hirth

Submission date: 09-Aug-2024 02:25AM (UTC-0500)
Submission ID: 2429426778
File name: e_arrangement_at_moderate_Reynolds_number__A_numerical_study.pdf (1.41M)
Word count: 14623
Character count: 72384

Physics of Fluids

RESEARCH ARTICLE | MAY 10 2023

Vortex-induced vibration of two circular cylinders in a side-by-side arrangement at moderate Reynolds number: A numerical study

Yosua Heru Irawan ; Syed Ahmad Raza ; Chern Ming-Jyh (陳明志)

Physics of Fluids 35, 055126 (2023)
https://doi.org/10.1063/5.0139301

Physics of Fluids ARTICLE pubs.aip.org/aip/phf

Vortex-induced vibration of two circular cylinders in a side-by-side arrangement at moderate Reynolds number: A numerical study

Cite as: Phys. Fluids 35, 055126 (2023); doi: 10.1063/5.0139301
Submitted: 19 December 2022 · Accepted: 27 April 2023 ·
Published Online: 10 May 2023

Yosua Heru Irawan,[1] Syed Ahmad Raza,[2] and Ming-Jyh Chern (陳明志)[1,a)]

AFFILIATIONS

[1]Department of Mechanical Engineering, National Taiwan University of Science and Technology, Taipei 106335, Taiwan
[2]Department of Mechanical Engineering, NED University of Engineering & Technology, Karachi 124087, Pakistan

[a)]Author to whom correspondence should be addressed: mjchern@mail.ntust.edu.tw

ABSTRACT

Vortex-induced vibration (VIV) of two transversely vibrating cylinders in a side-by-side (SBS) arrangement is numerically investigated using a combination of direct-forcing immersed boundary and large eddy simulation techniques. The VIV responses of vibrating SBS cylinders at two reduced velocities ($U_R^* = 4.0$ and 6.0) are studied for a range of gap ratio $1.0 \leq g^* \leq 3.0$. Moreover, the influence of mass ratio, damping ratio, and Reynolds number in the amplitude response and efficiency of VIVACE (Vortex-Induced Vibration for Aquatic Clean Energy) from vibrating SBS cylinders are investigated at moderate Reynolds numbers (Re = 1000 and 10 000). The optimal gap ratio for $U_R^* = 4.0$ is in the range of $1.0 \leq g^* \leq 1.2$. Larger than this range, the VIV responses are close to single-cylinder responses. At $U_R^* = 6.0$, all gap ratios show lower responses than a single-cylinder case. The vibrating SBS cylinder with a larger damping ratio results in higher maximum VIVACE efficiency with a narrower U_R^* range for significant efficiency. With almost the same amplitude response, the SBS cylinders with a lower mass ratio result in lower VIVACE efficiency. Using the same mass-damping parameters, it appears that a low mass ratio could be desirable to increase the U_R^* range of significant VIVACE efficiency and pick the proper damping ratio to reach a high value of maximum VIVACE efficiency. The effect of flow conditions on the amplitude response and VIVACE efficiency of vibrating SBS cylinders with the same VIV parameters is not significant.

I. INTRODUCTION

Vortex-induced vibration (VIV) of bluff bodies has been intensively studied as an attractive fluid–structure interaction (FSI) problem in recent decades.[1–5] The circular cylinder is one of the most common bluff bodies in engineering applications, such as risers, heat exchangers, chimneys, and so on. When fluid flow passes an elastically mounted cylinder, a cyclical sequence of vortices is released. Whenever the frequency of these vortices approaches the natural frequency of the vibrating cylinder, the cylinder will turn into synchronization with the fluid flow. This phenomenon occurs in a range of reduced velocity,[5] which is defined as $U_R^* = U_\infty/f_n D$, where U_∞ represents the uniform velocity, f_n represents the natural frequency of the vibrating cylinder, and D represents the cylinder diameter. In this situation, the vortex-shedding frequency f_v is locked into the vibration frequency of cylinder f_s, and these frequencies will synchronize with the natural frequency so that $f^* = f_v/f_n = f_s/f_n \approx 1.0$.[6] This regime is known as a lock-in region. Some VIV studies found a soft lock-in region, where the frequency ratio is not exactly equal to one.[7–9] In these regions, the frequency ratio remains almost constant over the range of reduced velocity, and the vibration amplitude becomes very large. VIV is usually known for its destructive effect in engineering applications with fluid flow past a bluff body because it can cause fatigue damage. In such types of cases, the goal is to reduce VIV so that structural integrity can be assured. In contrast to these applications, several recent studies have focused on enhancing VIV phenomena for use in energy harvesting devices, such as VIVACE (Vortex Induced Vibration for Aquatic Clean Energy). The VIVACE converter is designed to generate power by harnessing the potentially destructive effects of VIV, which is contrary to the past efforts that mostly concentrated on avoiding VIV.[10]

When dealing with the problem of multiple cylinders, the responses for both cylinders are fairly complex, and proximity intervention or a pairing of both could appear depending on the gap between cylinders. Recent comprehensive reviews of the interaction of

multiple cylindrical structures within a fluid flow can be found in the following articles.[11–13] Due to their practical importance in engineering applications, two cylinders in a side-by-side (SBS) arrangement are one of the most commonly encountered in multiple-cylinders configurations. Kang[14] investigated the characteristics of the flow past two cylinders in the SBS arrangement at a low Reynolds number using a two-dimensional (2-D) numerical simulation. This study showed that the gap between cylinders had a significant effect on the characteristics of drag and lift. In addition, the wake pattern and vortex shedding frequency were also strongly influenced by the gap between cylinders. The wake patterns behind the cylinders were classified into six patterns, namely, anti-phase-synchronized, in-phase-synchronized, flip-flopping, single bluff-body, deflected, and steady wake pattern. Each pattern has different fluid force characteristics.

Once the SBS cylinders are elastically mounted or allowed to vibrate freely, the gap between cylinders has a significant effect on the VIV responses. The current knowledge about VIV of two circular cylinders in the SBS arrangement is still far from complete because of several influencing factors, such as the gap ratio ($g^* = g/D$, where g represents the gap or surface-to-surface distance between two cylinders), the mass ratio ($m^* = 4m_s/\pi\rho D^2 L$, where m_s represents the cylinder mass, ρ represents the fluid density, and L represents the spanwise length of the cylinder), the damping ratio ($\zeta = c/(2\sqrt{m_s k})$, where c and k represent the damping and stiffness of the structure and the Reynolds number ($\mathrm{Re} = U_\infty D/\nu$, where ν represents the kinematic viscosity of fluid). A number of 2-D numerical studies of the VIV of two circular cylinders in the SBS arrangement have been carried out to observe the VIV responses of circular cylinders when both are free to vibrate. Chen *et al.*[15] used a 2-D numerical simulation to observe the VIV responses and wake pattern of two elastically supported SBS cylinders with $g^* = 1.0$–4.0, $\mathrm{Re} = 100$, and $m^* = 2.0$. The observations were made in the range of $3.0 \leq U_R^* \leq 10.0$. Furthermore, $\zeta = 0.0$ was used to obtain the maximum vibration amplitude. They divided the wake patterns into six groups, namely, irregular, in-phase flip-flopping, out-of-phase flip-flopping, in-phase-synchronized, anti-phase-synchronized, and biased-anti-phase-synchronized. Each of these patterns resulted from a different combination of gap ratio and reduced velocity. Moreover, using the same numerical method and VIV parameters, Chen *et al.*[16] investigated hysteresis and asymmetric vibration phenomena in the vibrating SBS cylinders with $g^* = 1.5$ and $\mathrm{Re} = 80$–125. Asymmetric vibration is distinguished by the inequality of vibration amplitudes of two cylinders, while symmetric hysteresis occurs when different vibration responses are obtained using increasing or decreasing initial conditions. The blockage ratio and the downstream length of the computational domain have a strong influence on asymmetric vibration and symmetric hysteresis. Chen *et al.*[17] extended the earlier study to investigate wake patterns. In this study, smaller increments of reduced velocity and gap ratio were used, requiring more than 1500 simulation cases to complete. The results were eight distinct wake patterns in the laminar flow regime, which can be used as a reference for similar research on transition or turbulent flow regimes. Chen *et al.*[18] investigated the VIV of two vibrating SBS cylinders. All cylinders are allowed to vibrate only in the cross-flow direction. The simulation parameters for this study were $\mathrm{Re} = 60$–200, $g^* = 1.0$–4.0, $U_R^* = 2.0$–10.0, $m^* = 2.0$–20.0, and $\zeta = 0.0$. For the case with $g^* < 1.3$, they reported a very strong interaction between the cylinders, as seen by the relatively larger vibration amplitudes and fluid forces. For the case with $g^* > 2.5$, the vibration response was almost the same as in the case of a single cylinder. In other words, the interaction between SBS cylinders was very small.

For three-dimensional (3-D) numerical simulation, Liu and Jaiman[19] numerically investigated the VIV of an upper circular cylinder in the SBS position and kept a lower cylinder in a stationary structure. This simulation was performed in the range of Reynolds number $100 \leq \mathrm{Re} \leq 500$ with the following VIV parameters: $m^* = 10.0$, $\zeta = 0.01$, and $U_R^* = 0.0$–10.0. The range of gap ratio, $0.3 \leq g^* \leq 3.0$, was used to investigate the VIV responses. An early onset of lock-in has been found for the vibrating cylinder (upper cylinder). Furthermore, a greater interference between the gap flow and the vibrating cylinder was found to affect the energy transfer between the flow and the cylinder while reducing the lock-in range. When the SBS cylinders are rigidly coupled, the wakes and vibration responses become more complex. Munir *et al.*[20] investigated the VIV responses of two rigidly coupled cylinders in the SBS arrangement using the 3-D numerical simulation. In this study, they used $m^* = 2.0$, $\zeta = 0.0$, $U_R^* = 1.0$–20.0, and $\mathrm{Re} = 1000$. They performed the investigation in the range of $0.5 \leq g^* \leq 3.0$ and discovered that for a small gap ratio, the range of high vibration amplitude response is divided into two regions: lock-in and sub-harmonic. The sub-harmonic region is a region in which the frequency of oscillation is half the resonant frequency of the lift coefficient. It was found that for $g^* = 0.5$, the interaction between cylinders was very strong, as characterized by a longer duration of the lock-in region and a larger amplitude. Moreover, for $g^* = 3.0$, the response of two cylinders was found to be similar to the response of the single cylinder.

The VIVACE system consists of multiple vibrating cylinders immersed in the water flow. As the water flows past the vibrating cylinders, it creates vortices that cause the cylinders to vibrate. This vibration is, then, converted to electrical energy using a linear generator or other energy conversion device. Vortex-induced vibration has the potential to provide a renewable and reliable source of energy. It has the added benefits of being relatively low-impact and environmentally friendly, as it does not involve the use of dams or other structures that can disrupt the natural flow of water. There are still some difficulties to be resolved in order to make vortex-induced vibration a practical and efficient source of renewable energy, such as improving the efficiency of energy conversion and developing robust and durable devices that can withstand the harsh conditions of the aquatic environment. Recently, Lv *et al.*,[21] Ding *et al.*,[22] Lee *et al.*,[23] Yuan *et al.*,[24] and Li *et al.*[25] conducted several experimental and computational investigations on VIVACE to explore the performance of multiple cylinders in a tandem arrangement. According to these studies, there is a potential for investigating the VIV response of the side-by-side (SBS) cylinders, especially, the features of the SBS configuration for optimizing the performance of a VIVACE system.

According to the studies described above, it is important to note that several parameters, such as the gap ratio, mass ratio, damping ratio, and reduced velocity, have strong effects on the VIV responses of vibrating circular cylinders in the SBS arrangement. Over the last few years, several studies of two freely vibrating cylinders in the SBS arrangement have been intently investigated by Chen *et al.*[15–18] All of these studies used 2-D numerical simulation to get the solution from the laminar flow regime with $\mathrm{Re} \leq 200$. A number of studies using

3-D numerical simulations at moderate Reynolds numbers, such as Liu and Jaiman[19] and Munir *et al.*,[20] have not focused on the case of freely vibrating cylinders in the SBS arrangement. Because of the practical importance in engineering applications, there is an opportunity to study the response of two transversely vibrating cylinders in the SBS arrangement using 3-D numerical simulation. In the present work, a 3-D numerical simulation of two transversely vibrating cylinders in the SBS arrangement is performed at moderate Reynolds numbers. The present numerical investigation is divided into two sections. The first investigation focuses on the influence of gap ratios in the VIV responses of SBS cylinders at $\mathrm{Re} = 1000$. The numerical investigation is conducted at $U_R^* = 4.0$ and 6.0 with $m^* = 10.0$ and $\zeta = 0.01$. The VIV responses of the two cylinders, such as amplitude and frequency, are studied for a range of gap ratio $1.0 \le g^* \le 3.0$. In addition, the correlation of VIV responses between the two vibrating cylinders, in particular the displacement, is also analyzed to determine the behavior of the two cylinders during vibration. Moreover, the efficiency of energy conversion is analyzed to evaluate the potential energy conversion of SBS cylinders in the VIVACE system. The second investigation focuses on the influence of VIV parameters and flow conditions in the amplitude response and VIVACE efficiency of SBS cylinders for a range of reduced velocities. This investigation is performed in the range of $2.0 \le U_R^* \le 10.0$ with the following parameters: $g^* = 1.2$; $m^* = 4.0$; and 10.0; $\zeta = 0.01$, 0.025, 0.035; and 0.0625; and $\mathrm{Re} = 1000$ and 10 000. According to the selected mass and damping ratios, the range of mass-damping parameter for this investigation is $0.04 \le m^*\zeta \le 0.625$. The previous study conducted by Barrero-Gil *et al.*[26] also used a similar mass-damping parameter to investigate the flow energy extraction from VIV at moderate Reynolds numbers (up to 10 000). In addition, Liu and Jaiman[19] and Chen *et al.*[27] also employed the same U_R^* range to study the VIV responses of vibrating SBS cylinders.

II. NUMERICAL METHODOLOGY

A. Fluid–structure interaction (FSI) modeling

In this present study, it is assumed that the fluid flow is incompressible and governed by the non-dimensional filtered continuity and Navier–Stokes equations,

$$\frac{\partial \bar{u}_i}{\partial x_i} = 0; \quad i, j = 1, 2, 3, \tag{1}$$

$$\frac{\partial \bar{u}_i}{\partial t} + \bar{u}_j \frac{\partial \bar{u}_i}{\partial x_j} = -\frac{\partial \bar{p}}{\partial x_i} + \left(\frac{1}{\mathrm{Re}} + \frac{\nu_t}{U_\infty D}\right) \frac{\partial^2 \bar{u}_i}{\partial x_j^2} + \eta f_i, \tag{2}$$

where $(x_1, x_2, x_3) = (x, y, z)$ represent three directions in the Cartesian coordinate system, and $(\bar{u}_1, \bar{u}_2, \bar{u}_3) = (\bar{u}, \bar{v}, \bar{w})$ are the non-dimensional filtered velocity components in the x, y, and z directions. The terms, $\bar{p}$ and ν_t, are the non-dimensional filtered pressure and the turbulent viscosity (U_∞ and D are used to normalize ν_t). The Reynolds number, $\mathrm{Re} = U_\infty D/\nu$, in the right-hand side of Eq. (2) is used as an input parameter in order to specify the flow condition in this simulation. A direct-forcing immersed boundary (DFIB) technique is employed to perform the fluid–structure interaction (FSI) simulation. A volume-of-solid (VoS) function, η, is introduced here to allow the interaction between a moving structure and fluid flow around it. The calculation of η is performed in all computational grids to identify the immersed solid structure. Here, $\eta = 1$ implies the computational grid filled by the solid structure, $\eta = 0$ means the computational grid occupied by the fluid, and $0 < \eta < 1$ represents a virtual wall boundary of the solid structure. In order to get a finer virtual wall boundary, a sub-grid method is used to recalculate VoS at $0 < \eta < 1$. This method has been applied successfully to capture the virtual wall boundary of 3-D structures.[28,29] Furthermore, $(f_1, f_2, f_3) = (f_x, f_y, f_z)$ in the last term of Eq. (2) represent the virtual forces for the immersed solid structure in the x, y and z directions, and this term will only be calculated on the computational grids with $\eta > 0$.

Zhao *et al.*[5] studied the transition flow regime from laminar to turbulent on a freely vibrating cylinder and concluded that the wake behind the vibrating structure becomes turbulent if $\mathrm{Re} \ge 300$. In order to model the turbulent wake in this present investigation, large eddy simulation (LES) with the Smagorinsky–Lilly model is used. The turbulent viscosity, ν_t in Eq. (2), is calculated using the following equations:

$$\nu_t = (C_s \Delta)^2 |\bar{S}|, \tag{3}$$

$$\bar{S} = \sqrt{\bar{S}_{ij}\bar{S}_{ij}}, \tag{4}$$

where S_{ij} represents the rate of strain of resolved velocity scale, $\Delta = (\Delta x \Delta y \Delta z)^{\frac{1}{3}}$ is the filter width calculated from finer computational grids near the vibrating structure, and C_s represents the Smagorinsky constant. The present investigation employs a constant value of $C_s = 0.1$. The calculation of turbulent viscosity is performed for all computational grids. As long as the gradient of resolved velocity scale is greater than zero, Eq. (3) introduces turbulent fluctuation at the virtual wall boundary, which must be canceled in order to enforce the no-slip boundary condition. In this present study, the Van-Driest damping function f_d is incorporated in the calculation of turbulent viscosity. Hence, Eq. (3) can be rewritten as

$$\nu_t = (f_d C_s \Delta)^2 |\bar{S}|, \tag{5}$$

$$f_d = 1 - \exp\left(-\frac{y^+}{25}\right), \tag{6}$$

where the dimensionless wall distance, y^+, is calculated from the finest grid size near the vibrating structure. Equation (5) is only used to calculate the turbulent viscosity on computational grids with $0 < \eta < 1$ (virtual wall boundary). The combination of DFIB-LES techniques has been proven to predict the flow field in the case of flow past a circular cylinder at $\mathrm{Re} = 3900$.[29]

The freely vibrating structure is modeled by the following non-dimensional mass-spring-damper equation:

$$\frac{\mathrm{d}^2 Y^*}{\mathrm{d}t^2} + \frac{4\pi\zeta}{U_R^*}\frac{\mathrm{d}Y^*}{\mathrm{d}t} + \left(\frac{2\pi}{U_R^*}\right)^2 Y^* = \frac{2C_L(t)}{\pi m^*}, \tag{7}$$

where Y^* represents the non-dimensional displacement of the vibrating structure in the cross-flow direction. Further, Eq. (7) is split into Eqs. (8) and (9) in order to get the numerical solution,

$$\frac{\mathrm{d}Y^*}{\mathrm{d}t} = s_y, \tag{8}$$

$$\frac{\mathrm{d}s_y}{\mathrm{d}t} = \frac{2C_L(t)}{\pi m^*} - \frac{4\pi\zeta}{U_R^*} s_y - \left(\frac{2\pi}{U_R^*}\right)^2 Y^*, \tag{9}$$

where s_y represents the velocity of vibrating structures in the cross-flow direction. Furthermore, this method has also been used to model

VIV simulations of a single cylinder and multiple cylinders with Reynolds numbers up to 1000.[30,31] More details about parameters involved in Eq. (7) will be explained clearly in Subsection II C.

B. *TIGER-C* solver and computational environment

An in-house solver based on the C++ programing language, named TIGER-C, is used to perform the present numerical study. This solver employs the DFIB-LES techniques on which the governing equations in Eqs. (1) and (2) are discretized using the finite volume method with a staggered grid. The projection algorithm is used to solve the governing equation of the incompressible fluid flow in Eqs. (1) and (2). In order to advance the flow field, a time-splitting technique with three steps is used. In the first stage, the velocity is updated from the n-th time level, $\bar{u}_i^n$, to the first intermediate level $\bar{u}_i^*$ by solving the advection and diffusion terms. Following that, this procedure may be expressed in the following forms:

$$\frac{\bar{u}_i^* - \bar{u}_i^n}{\Delta t} = \frac{1}{12}\left[23A^n - 16A^{n-1} + 5A^{n-2}\right], \tag{10}$$

where A represents the advection and diffusion terms in Eq. (2). The quadratic upstream interpolation for the convective kinematic (QUICK) scheme is used to discretize the advection term, and for the diffusion term, the second-order central difference scheme is used to calculate the velocity gradient in Eq. (4). This step uses the third-order Adams–Bashforth method for the temporal discretization, as shown in Eq. (10). For the second stage, the first intermediate velocity, $\bar{u}_i^*$, is updated to the second intermediate velocity $\bar{u}_i^{**}$ by solving pressure term,

$$\frac{\bar{u}_i^{**} - \bar{u}_i^*}{\Delta t} = -\frac{\partial \bar{p}^{n+1}}{\partial x_i}. \tag{11}$$

Taking the divergence on both sides and substituting the conservation of mass, $\frac{\partial \bar{u}_i^{**}}{\partial x_i} = 0$, in Eq. (11) yield the pressure Poisson equation,

$$\frac{\partial^2 \bar{p}^{n+1}}{\partial x_i^2} = \frac{1}{\Delta t}\frac{\partial \bar{u}_i^*}{\partial x_i}. \tag{12}$$

The bi-conjugate gradient stabilized (Bi-CGSTAB) method is used to solve the pressure field in Eq. (12). After Eq. (12) is resolved, the second intermediate velocity in Eq. (11) can be updated. The third stage is updating the flow field to $\bar{u}_i^{n+1}$ by solving the virtual force term,

$$\frac{\bar{u}_i^{n+1} - \bar{u}_i^{**}}{\Delta t} = \eta f_i^{n+1}. \tag{13}$$

In Eq. (2), the virtual force term, ηf_i, represents the effect of a solid structure on a fluid flow. This virtual force maintains or moves a stationary or moving structure. To keep the no-slip boundary condition for the solid structure, the virtual force in the solid structure should guarantee that fluid velocity, $\bar{u}_i$, is equal to the structure velocity, s_i, at the $(n+1)^{th}$ time step ($\bar{u}_i^{n+1} = s_i^{n+1}$), where ($s_1$, s_2, $s_3 = s_x$, s_y, s_z) represent the structure velocity in the x, y, and z directions. Hence, the virtual force is the rate of change in momentum of a solid structure and is comparable to the difference between the structure velocity at the $(n+1)^{th}$ time step and the fluid velocity at the n^{th} time step,[32]

$$\eta f_i^{n+1} = \eta\frac{\bar{u}_i^{n+1} - \bar{u}_i^n}{\Delta t} = \eta\frac{s_i^{n+1} - \bar{u}_i^n}{\Delta t}. \tag{14}$$

This virtual force only exists on the computational grids occupied by solid structures ($\eta > 0$). The governing equations for structure motion, Eqs. (8) and (9), are solved by using the fourth-order Runge–Kutta method. The numerical solutions from Eqs. (8) and (9) are used to update the location of η and to calculate the virtual force in Eq. (14). This step ensures two ways fluid–structure interaction (FSI) modeling between the fluid flow and the vibrating structure. Furthermore, Simpson's 1/3 rule is used to integrate the virtual force in all computational grids occupied by solid structures. The presented algorithm was successfully used to simulate FSI problems for 2-D and 3-D solid structures in laminar and turbulent flow regimes.[28,30,31,33–35]

The numerical computations are carried out on the TAIWANIA-3 supercomputer at the National Center for High-performance Computing (NCHC), Taiwan. Each computing node has two Intel® Xeon® Platinum 8280 2.4 GHz (28 Cores/CPU). The Open Multi-Processing (OpenMP) method is used to divide the computational load for each core in order to optimize multi-core processors. TIGER-C achieves a maximum speedup of more than 14 times, or parallel calculations using multi-cores in this solver are 14 times faster than serial calculations using single core. The source code for this numerical solver is compiled using GNU Compiler Collection GCC 9.4.0. The time increment $\Delta t = 0.001$ is used in this investigation, and the Courant–Friedrichs–Lewy (CFL) criterion is less than 0.05. This solver takes 27–40 h to achieve $t^* = 2000$ at Re = 1000 using 28 cores. The computing time required to attain $t^* = 2000$ in the case study with Re = 10 000 is 51–67 h using 28 cores. This research includes 99 3-D numerical simulations, including 82 cases for the primary investigation, ten cases for the validation section, and seven cases for the grid independence test. For the primary study, there are 16 cases for VIV of SBS cylinders with various gap ratios, 44 cases for VIV of SBS cylinders with different VIV parameters at Re = 1000, and 22 cases for VIV of SBS cylinders with varying VIV parameters at Re = 10 000.

C. Computational domain and simulation parameters

Figure 1 shows the details of the computational domain for VIV simulation incorporating two cylinders in the SBS arrangement. The SBS cylinders are located at 20D behind the inlet domain. This structure arrangement forms 20D upstream flow direction distance, x_u, and 30D downstream flow direction distance, x_d. According to the previous study performed by Prasanth *et al.*,[36] the downstream flow direction distance, x_d, beyond 25.5D had no significant effect on the near wake flow and the cylinder response. The length of the domain in the

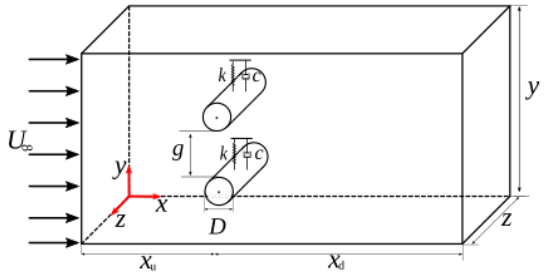

FIG. 1. Computational domain.

cross-flow direction, y, is $40D$, so the blockage ratio for this present study, $2D/y$, is around 5%. Previous VIV simulations conducted by Prasanth *et al.*[37] also employed the same blockage ratio. The spanwise length, z, for this simulation is $3D$, and the periodic boundary condition is imposed at two spanwise boundaries. The shorter spanwise length can be used with this periodic boundary condition since the flows at the two spanwise boundaries are the same when the periodic boundary condition is employed.[5] Kondo[38] also used the periodic boundary condition with short spanwise length ($z = 2.5D$) to perform a 3-D numerical investigation of multiple cylinders. The free-stream and zero-gradient boundary conditions are utilized at the inlet and outlet of the computational domain. At the two cross-flow boundaries, the symmetry boundary condition is applied, where the velocity component in the direction perpendicular to the boundary is zero. Finally, the no-slip boundary condition is imposed on the cylinder surfaces. The combination of boundary conditions used in this study was successfully implemented by Raza *et al.*[29] to predict the physical phenomena of flow past a circular cylinder in the turbulent flow using similar DFIB-LES techniques. Liu and Jaiman,[19] Pastrana *et al.*,[39] and Wang *et al.*[40] also used a similar combination of boundary conditions to simulate 3-D VIV simulation. Figure 2 shows details of the grid composition of this simulation. The fine grids are uniformly distributed near the cylinder surfaces to capture solid boundaries, near wake and displacement of the vibrating cylinders. In the far wake region, the grids will not be uniformly distributed to the streamwise and cross-flow directions until the end of the computational domain. The non-uniform grid expansion in this study is constructed based on a previous study conducted by Chern *et al.*[33] The uniform grids are also applied in the spanwise direction.

Table I shows the input parameters in this present study. Herein, U_∞, D, ν, t, ρ, and g refer to the free stream velocity, cylinder diameter, kinematic viscosity of a fluid, simulation time, fluid density, and gap between cylinders, respectively. The structure parameters for this simulation are structure damping c, structure mass m_s, structure stiffness k, spanwise length L, and structure natural frequency f_n. Table II shows the output parameters for detailed analysis. The resultant force is calculated from the integral of the virtual force exerted on a solid structure. This integration process employs Simpson's 1/3 rule. The subscripts x and y indicate the direction of the virtual force in the in-flow and cross-flow. Y^*_{rms}, f_v, and f_s represent the root mean square of dimensionless transverse displacement, vortex-shedding frequency, and vibration frequency of the structure. Fast Fourier transform (FFT) and Hilbert–Huang transform (HHT) are used to analyze those frequency responses. Due to the turbulent wake behind the cylinder, some fluctuations in the time-series data will sometimes induce multiple harmonics. This current study employs fast Fourier transform (FFT) to get the dominant harmonic of the time-series signal and then

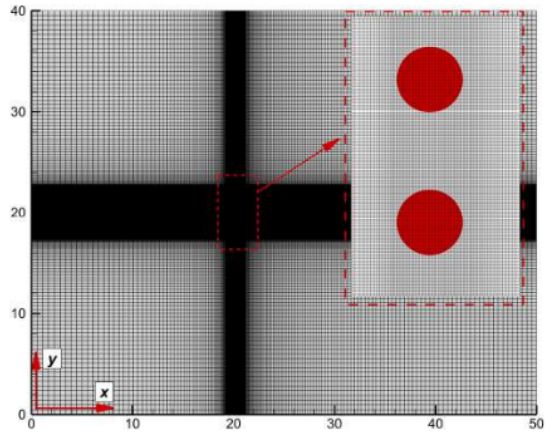

FIG. 2. Grid composition (side view of the computational domain).

TABLE I. Dimensionless parameters for the VIV simulation of SBS cylinders (input parameters).

Parameter	Value	Description
$\text{Re} = \frac{U_\infty D}{\nu}$	1000 and 10 000	Reynolds number
$t^* = \frac{tU_\infty}{D}$	0–2000	Time
$g^* = \frac{g}{D}$	1.0–3.0	Gap ratio
$\zeta = \frac{c}{2\sqrt{m_s k}}$	0.01, 0.025, 0.035, and 0.0625	Damping ratio
$m^* = \frac{4m_s}{\pi\rho D^2 L}$	4.0 and 10.0	Mass ratio
$U_R^* = \frac{U_\infty}{f_n D}$	2.0–10.0	Reduced velocity
$f_n^* = \frac{f_n D}{U_\infty}$	0.1–0.5	Natural frequency

TABLE II. Derived dimensionless parameters for detailed analysis (output parameters).

Parameter	Description
$C_D = \frac{2f_x}{\rho U_\infty^2 DL}$	Drag coefficient
$C_L = \frac{2f_y}{\rho U_\infty^2 DL}$	Lift coefficient
$Y^* = \frac{Y}{D}$	Transverse displacement
$A^* = \frac{A}{D} = \sqrt{2}Y^*_{\text{rms}}$	Amplitude response
$f_v^* = \frac{f_v D}{U_\infty}$	Vortex-shedding frequency (Strouhal frequency)
$f_s^* = \frac{f_s D}{U_\infty}$	Structure frequency
$A_t(t^*)$	Autocorrelation function [Eq. (15)]
$\eta_{V\,IV\,ACE}$	VIVACE efficiency [Eq. (20)]

verify the frequency in the Hilbert spectrum produced by Hilbert–Huang transform (HHT). HHT is divided into two sections: empirical mode decomposition and Hilbert spectral analysis. This technique reveals time-frequency-amplitude representations for non-stationary data analysis. Hilbert spectrum provides information about the instantaneous frequency and instantaneous amplitude along the time-series data. The autocorrelation function $A_t(t^*)$ is used to determine the correlation of the displacement response between the lower and upper cylinders. The autocorrelation $A_t(t^*)$ for two time series data is calculated from the following equations:[41,42]

$$A_t(t^*) = \frac{\overline{Y^U Y^L}}{\overline{(Y^U)^2}}, \tag{15}$$

$$\overline{Y^U Y^L} = \lim_{t_f \to \infty} \frac{1}{t_f - t_i} \int_{t_i}^{t_f} Y^U(t^*) Y^L(t^*) \mathrm{d}t^*, \tag{16}$$

$$\overline{(Y^U)^2} = \lim_{t_f \to \infty} \frac{1}{t_f - t_i} \int_{t_i}^{t_f} (Y^U(t^*))^2 \mathrm{d}t^*, \tag{17}$$

where t_i and t_f represent the initial time and final time, and the superscripts U and L stand for upper and lower cylinders, respectively. If Y^U is the same as Y^L, then $A_t(t^*) = 1$. This condition represents an in-phase state. Moreover, $A_t(t^*) = -1$ when Y^U and Y^L are equal in magnitude but opposite in signs. Hence, Y^U and Y^L are in an anti-phase state. If Y^U is completely uncorrelated to Y^L, then $A_t(t^*)$ will become close to 0. The efficiency of VIVACE represents the amount of the extracted energy from the available energy in the fluid flow. The following equation evaluates the converted power from the vibrating cylinder in the VIVACE system:[25,43]

$$P_{VIVACE} = 8\pi^3 (m_s + m_a) \zeta A f_s f_n, \tag{18}$$

where m_s is the structure mass, m_a is the added mass, ζ is the damping ratio, A is the vibration amplitude, f_s is the vibration frequency, and f_n is the natural frequency in a quiescent water. In this study, the value of m_a is equal to the displaced fluid mass $m_d = \pi/(4\rho D^2 L)$,[43,44] where ρ, D, and L represent the fluid density, cylinder diameter, and cylinder length. The displaced fluid mass is used to normalize the structure mass and added mass in Eq. (18); hence, $(m_s + m_a) = (m^* + 1)$, where $m^* = m_s/m_d$ is the mass ratio. The cylinder diameter is used as a reference length to normalize the vibration amplitude $A^* = A/D$. In order to normalize both frequencies in Eq. (18), the reference length D and reference velocity U_∞ are used; hence, $f_s^* = f_s D/U_\infty$ and $U_R^* = U_\infty/f_n D$. This study uses the reduced velocity U_R^* as the input simulation parameter. Using a constant Reynolds number, $\mathrm{Re} = U_\infty D/\nu$, the change in U_R^* means the changing f_n in quiescent water. The available power in a fluid flow is calculated by using the following equation:

$$P_{fluid} = \frac{1}{2} \rho U_\infty^3 (2A + D) L. \tag{19}$$

Here, the swept area of the vibrating cylinder $(2A + D)L$ is used, where A, D, and L are also normalized by using the reference length. In theory, the Betz limit, where the maximum value is 16/27, is equal to the maximum efficiency of extracting power by a fluid flow energy converter. Therefore, the efficiency of VIVACE is determined by the following equation:[25,44]

$$\eta_{VIVACE}(\%) = \frac{P_{VIVACE}}{P_{fluid} \times \text{Betz limit}} \times 100. \tag{20}$$

TABLE III. Grid independence study at $U_R^* = 4.0$ for investigation with $\mathrm{Re} = 1000$ (percentage error inside a bracket is calculated based on the finest grid).

Case	Δx Δy	y^+	Number of elements	A^*	f_s^*/f_n^*
Grid A	$0.050D$	5.13	281 880	0.3498 (27.98%)	0.8880 (1.81%)
Grid B	$0.025D$	2.56	1 115 730	0.4832 (0.51%)	0.9012 (0.35%)
Grid C	$0.020D$	2.05	1 722 825	0.4857	0.9044

D. Grid independence study

Table III presents the grid independence study at $U_R^* = 4.0$ for investigation with $\mathrm{Re} = 1000$. The output parameters represent the VIV responses from the lower cylinder only due to the identical VIV response of SBS cylinders. The previous numerical study also found this similar behavior.[18] Various grid compositions are used to model the transverse oscillations of SBS circular cylinders in order to find the grid independent results, especially for the free vibration of SBS circular cylinders. Herein, grid A, grid B, and grid C are composed of different grid spacings near the structures in the streamwise (Δx) and cross-flow (Δy) directions. The additional grid parameters, such as y^+ and the number of elements, are also calculated based on grid spacing near the structures. Furthermore, as the grid spacing decreases, y^+ decreases, and the total number of grids increases. The input VIV parameters are structure damping ratio ($\zeta = 0.01$) and mass ratio ($m^* = 10$). This grid independence study is performed with the constant gap ratio between cylinders, $g^* = 1$. Dimensionless vibration amplitude, A^*, and its frequency, f_s^*, are analyzed to justify the grid independence criteria. Grid B and grid C produce almost similar results with the largest difference of less than 1%. As a result, grid B is adopted in this present investigation at $\mathrm{Re} = 1000$ to get the accuracy of numerical results while also minimizing computational time.

Table IV presents the grid independence study at $U_R^* = 5.0$ for the investigation with $\mathrm{Re} = 10\,000$. The same mass, damping, and gap ratios as the previous grid-independent test are used. The differences

TABLE IV. Grid independence study at $U_R^* = 5.0$ for investigation with $\mathrm{Re} = 10\,000$ (percentage error inside a bracket is calculated based on the finest grid).

Case	Δx Δy	y^+	Number of elements	A^*	f_s^*/f_n^*
Grid A	$0.050D$	35.66	281 880	0.4482 (10.89%)	0.91 (1.09%)
Grid B	$0.025D$	17.83	1 115 730	0.4772 (5.13%)	0.9165 (0.38%)
Grid C	$0.020D$	14.26	1 722 825	0.5028 (0.04%)	0.92 (0.0%)
Grid D	$0.015D$	10.69	2 743 800	0.503	0.92

are the reduced velocity and the flow condition. An additional grid composition, grid D, is introduced here to investigate the VIV responses in a further grid refinement. The result of y^+ value is different due to the difference in the flow condition used in this grid independence study. The same amplitude and frequency responses of the lower cylinder are used to analyze the grid independence criteria. The results from grid C and grid D are quite close to each other, with the highest difference being less than 1%. Therefore, in order to get accurate numerical predictions while simultaneously reducing calculation time, grid C is employed in the current investigation at Re = 10 000.

Several researchers have proposed that additional assessments are needed to ensure the grid independence of the resolved scale simulations, such as LES.[45] Celik *et al.*[46] proposed a quality evaluation approach known as LES_IQ (LES index of quality) to analyze the accuracy of LES. A quality index is produced in this assessment based on a comparison of resolved scales in the computational domain with two distinct grid resolutions. For acceptable resolved scale simulation, a quality index equal to or better than 0.8 is suggested.[46] The following equations are used to perform the calculation of LES_IQ:[45]

$$\mathrm{LES\_IQ}_k^{\mathrm{coarse}} = 1 - \frac{|a_k \Delta_1^m|}{k_1^{\mathrm{res}} + a_k \Delta_1^m}, \tag{21}$$

$$\mathrm{LES\_IQ}_k^{\mathrm{fine}} = 1 - \frac{|a_k \Delta_2^m|}{k_2^{\mathrm{res}} + a_k \Delta_2^m}, \tag{22}$$

where subscripts 1 and 2 represent coarse and fine grids, m is associated with the accuracy of the adopted numerical scheme ($m = 3$ for the QUICK scheme), Δ is the filter length ($\Delta = (\Delta x \Delta y \Delta z)^{1/3}$), k^{res} is the resolved turbulence kinetic energy, and a_k is a coefficient that can be determined by performing the LES simulation with coarse and fine grid resolutions,

$$a_k = \frac{1}{\Delta_2^m}\left[\frac{k_2^{\mathrm{res}} - k_1^{\mathrm{res}}}{\left(\frac{\Delta_1}{\Delta_2}\right)^m - 1}\right]. \tag{23}$$

Figures 3 and 4 show the results for the LES_IQ assessment for flow past SBS cylinders at Re = 1000 and Re = 10 000. Four plot locations near SBS cylinders are selected to show the LES_IQ. Grid A and grid B are coarse and fine grid resolutions for the LES_IQ assessment at Re = 1000. For the LES_IQ assessment at Re = 10 000, grid A and grid C represent coarse and fine grid resolutions. As shown in Figs. 3 and 4, the results of LES_IQ for grid B (at Re = 1000) and grid C (at Re = 10 000) are within the suggested range of good LES simulation (LES_IQ > 0.8). According to these results, grid B and grid C are sufficient to perform the resolved scale simulation at Re = 1000 and Re = 10 000, respectively.

E. Validation case

To assess the capability of the TIGER-C solver under the higher Reynolds number condition, a validation case for VIV of a single cylinder is carried out. The VIV simulation is executed using the following VIV parameters: $m^* = 2.4$, $\zeta = 0.0054$, and $U_R^* = 1.0$–12.0 for the range of $900 < \mathrm{Re} < 12\,000$. The VIV simulation begins in an increasing-U_R^* condition to replicate the data sampling techniques in the published studies.

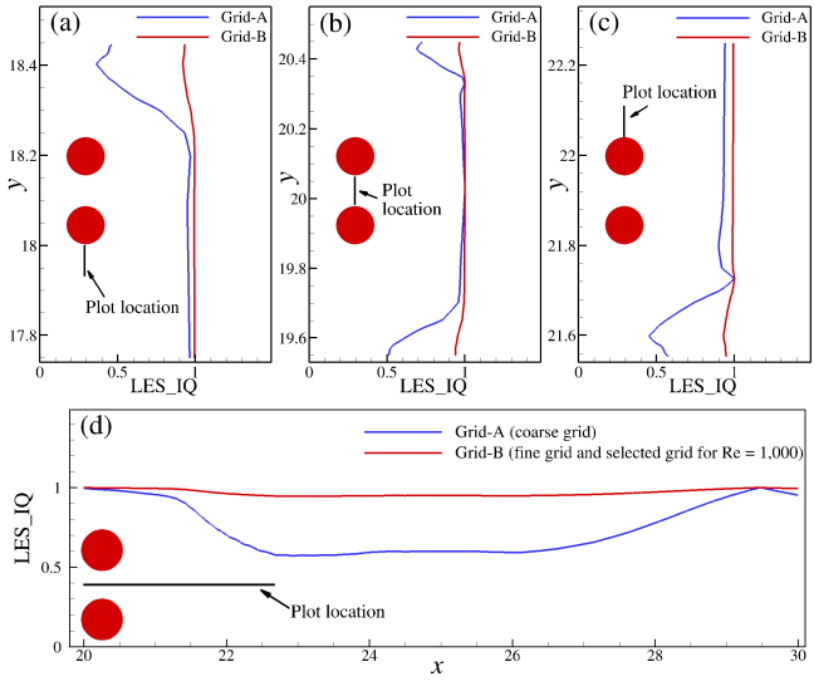

FIG. 3. Results for LES_IQ assessment for flow past SBS cylinders at Re = 1000: (a) lower plot line (x, y, $z = 20D$, $17.75D$–$18.5D$, $1.5D$), (b) gap plot line (x, y, $z = 20D$, $19.5D$–$20.5D$, $1.5D$), (c) upper plot line (x, y, $z = 20D$, $21.5D$–$22.25D$, $1.5D$), and (d) horizontal plot line (x, y, $z = 20D$–$30D$, $20D$, $1.5D$).

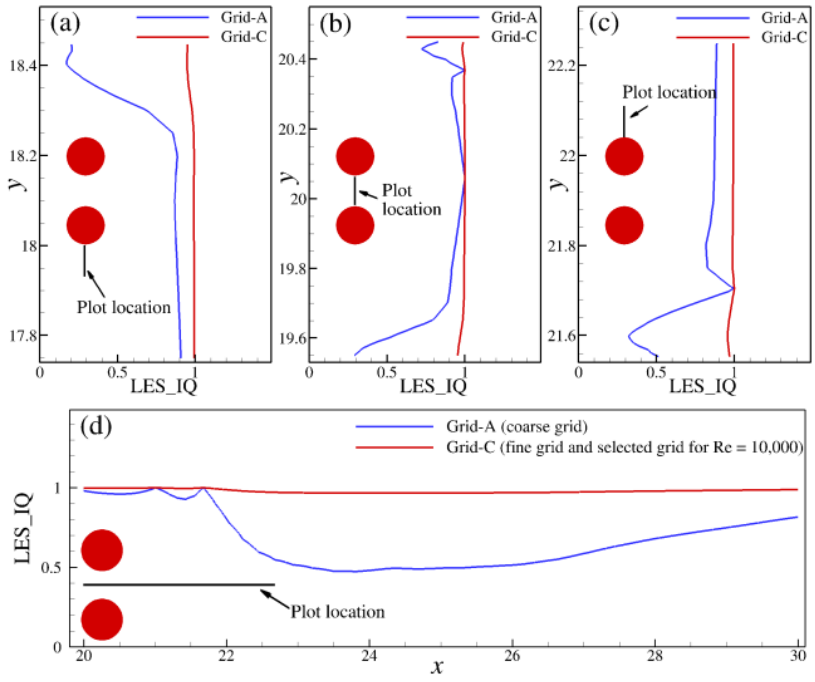

FIG. 4. Results for LES_IQ assessment for flow past SBS cylinders at Re = 10 000: (a) lower plot line (x, y, $z = 20D$, $17.75D$–$18.5D$, $1.5D$), (b) gap plot line (x, y, $z = 20D$, $19.5D$–$20.5D$, $1.5D$), (c) upper plot line (x, y, $z = 20D$, $21.5D$–$22.25D$, $1.5D$), and (d) horizontal plot line (x, y, $z = 20D$–$30D$, $20D$, $1.5D$).

Moreover, the VIV responses for the range of U_R^* and Re are shown as a normalized maximum amplitude, maximum lift coefficient, and maximum drag coefficient. Figure 5 shows the VIV responses of a single cylinder for the selected range of Reynolds numbers: (a) maximum amplitude, (b) maximum lift coefficient, and (c) maximum drag coefficient. The published results from Khalak and Williamson,[47] Guilmineau and Queutey,[48] Pan *et al.*,[49] Khan *et al.*,[50] and Matin Nikoo *et al.*[51] are used for comparison. Khalak and Williamson[47] used the measurement data to classify the VIV responses of a single cylinder into three distinct branches: initial, upper, and lower. When compared with the experimental result from Khalak and Williamson,[47] the current results are in good agreement at the beginning of the upper and lower branches. However, the present results are somewhat over-predicted in the initial branch and at the end of the lower branch. As shown in Fig. 5, none of the numerical solutions is able to provide an accurate prediction of the upper branch from the experiment measurement. The presence of a finite cylinder in the VIV experiment, which caused fluid flow between the cylinder tip and the channel wall, is one of the possible factors of this issue. The published results from 2-D RANS simulation,[49,50] in which the cylinder length impact is totally removed from the computation, shows a substantially distinct pattern of maximum amplitude on the upper branch, as presented in Fig. 5(a). Technically, the 3-D numerical simulation provides a more precise result, particularly in the case of turbulent flow. At the onset of the upper branch, both the present study and Matin Nikoo *et al.*[51] provide accurate numerical results. After that, both results are under-predicted until the termination of the upper branch. Possibly, the spanwise boundary condition is the cause of this disparity. For the spanwise boundary, the 3-D LES applies the periodic condition, whereas the 3-D RANS uses the symmetry condition. Both boundary conditions are clearly different from the physical condition in the VIV measurement conducted by Khalak and Williamson.[47] In general, the present numerical solver is capable of grasping all three branches of the VIV responses, in contrast to the earlier 2-D numerical studies, which have difficulty, primarily in the upper branch.

In order to validate the numerical method for multiple structures problem, the VIV of an upper cylinder in the SBS arrangement is selected as the benchmark case. Liu and Jaiman[19] investigated this case to analyze the influence of gap flow in the VIV of an upper cylinder in the SBS arrangement. The influence of gap flow in VIV is included by allowing an upper cylinder to vibrate freely in the cross-flow direction. In this validation case, the flow condition and VIV parameters are selected according to Liu and Jaiman[19] (Re = 500, $g^* = 0.8$, $m^* = 10.0$, $\zeta = 0.01$, and $U_R^* = 3.0$ to 9.0). Liu and Jaiman[19] solved this problem until $t^* = 350$ and employed time window $t^* = 250$ to 350 (20 vortex-shedding cycles) for the calculation of vibration responses. Twenty vortex-shedding cycles were also used in this study to calculate the vibration responses. This present study collected data until $t^* = 2000$ (more than 200 vortex-shedding cycles) and selected 20 vortex-shedding cycles from time-series data for validation cases. Figure 6 shows the validation results of (a) amplitude response and (b) frequency ratio of an upper cylinder in the SBS arrangement. The published result from Liu and Jaiman[19] is attached for comparison. The present results are in good agreement with those of Liu and Jaiman[19]

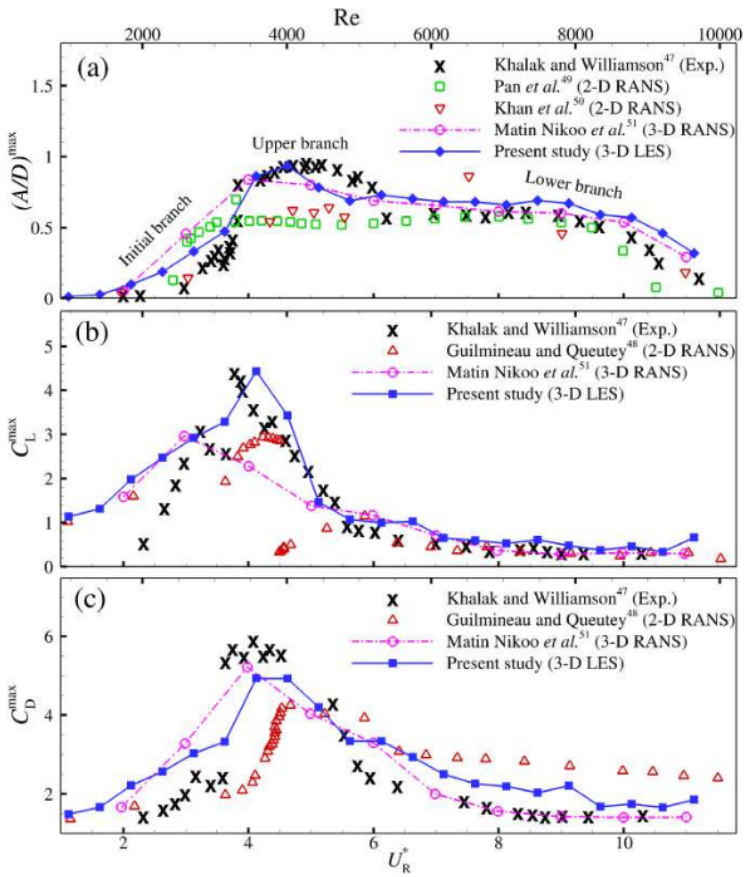

FIG. 5. VIV responses of a single cylinder for the selected range of Reynolds numbers: (a) maximum amplitude, (b) maximum lift coefficient, and (c) maximum drag coefficient. Published results from Khalak and Williamson,[47] Guilmineau and Queutey,[48] Pan *et al.*,[49] Khan *et al.*,[50] and Matin Nikoo *et al.*[51] are used for comparison.

in terms of the vibration amplitude and the frequency ratio, as demonstrated in Fig. 6. Both validation results show that the current solver is reliable and accurate. More validation examples are included in the previous investigations by the authors.[28,29,33,35]

III. RESULTS AND DISCUSSION

The results and discussion are divided into three sections. Section III A presents the instantaneous responses of the elastically mounted vibrating cylinder, such as displacement, frequency, and flow field. Section III B presents the results and discussion of the first investigation. The VIV responses of vibrating SBS cylinders at Re = 1000 are investigated in this section, including amplitude, frequency ratio, and the response correlation between two cylinders. Furthermore, the energy conversion efficiency is investigated to determine the potential energy conversion of SBS cylinders for the VIVACE system. The SBS cylinders are only allowed to vibrate in the cross-flow direction. The surface-to-surface spacing ratio or the gap ratio is in the range of $1.0 \leq g^* \leq 3.0$. The following VIV parameters are used: $U_R^* = 4.0$ and 6.0, $m^* = 10.0$, and $\zeta = 0.01$. The result from the 3-D VIV simulation of a single-cylinder with the same relevant parameters is presented for data comparison. The second investigation on the effect of VIV parameters and flow conditions on the amplitude response and the energy conversion efficiency of SBS cylinders over a range of reduced velocities are presented and discussed in Sec. III C. This section investigates the influence of mass ratio, damping ratio, and Reynolds number for various reduced velocities using the amplitude response and VIVACE efficiency of vibrating SBS cylinders with $g^* = 1.2$. This investigation is conducted with the following parameters: $m^* = 4.0$ and 10.0; $\zeta = 0.01$, 0.025, 0.035, and 0.0625; and Re = 1000 and 10 000, with U_R^* values from 2.0 to 10.0.

A. Time-series data and instantaneous flow field

Figure 7 shows the time-series data of (a) cylinder displacement and (b) lift coefficient from a single-cylinder case with the following parameters: $m^* = 10.0$, $\zeta = 0.01$, $U_R^* = 6$, and Re = 1000. In order to capture vibration responses in the VIV simulation at Re = 1000, at least 40 cycles of vibration are recorded.[5] All cases in this study are simulated until $t^* = 2000$, while the time duration for average calculation or the

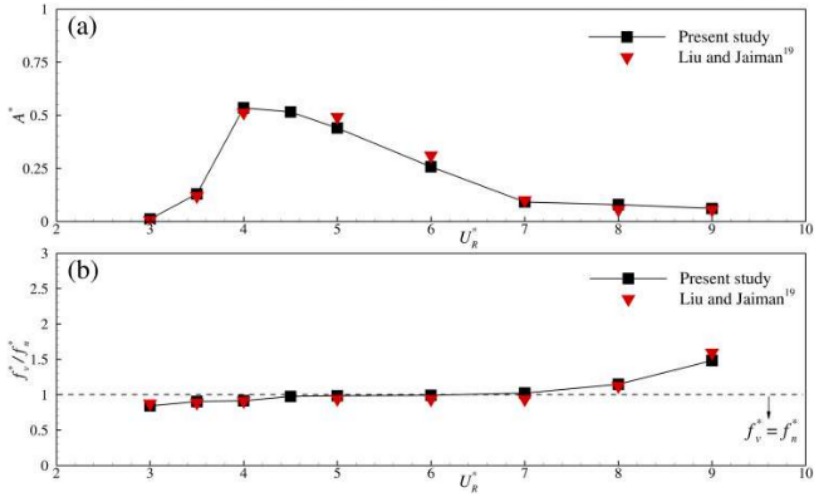

FIG. 6. Validation results of (a) amplitude response and (b) frequency ratio of an upper cylinder in the SBS arrangement. The published result from Liu and Jaiman[19] is attached for comparison.

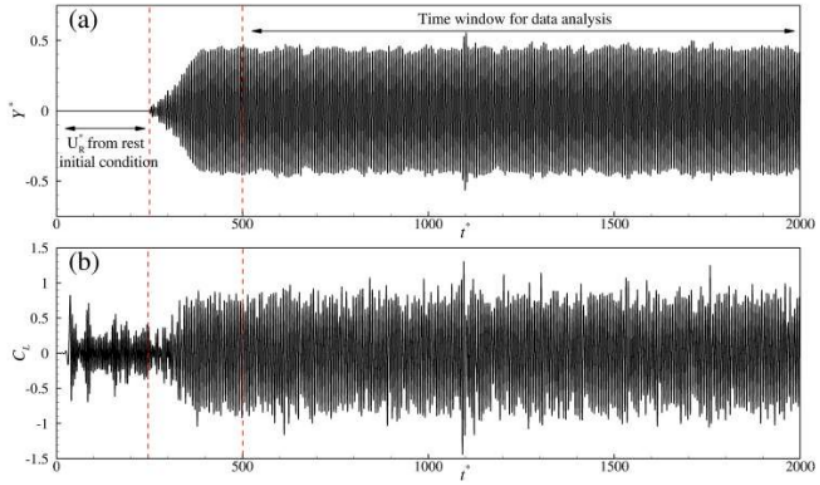

FIG. 7. Time-series data of (a) cylinder displacement and (b) lift coefficient from a single-cylinder case with the following parameters: $m^* = 10.0$, $\zeta = 0.01$, $U_R^* = 6$, and Re = 1000.

time window for data analysis is $t^* = 500$–2000, where the flow solution is fully established for flow statistics collection. The output simulation parameters, such as hydrodynamic forces and vibration responses, undergo at least 100 cycles in the adopted time window. This current study employs U_R^*-from-rest initial condition to start the VIV simulation at the constant Reynolds number. In this condition, the cylinder is maintained in a fixed position until $t^* = 250$. After this, the elastically mounted cylinder is enabled to vibrate as the lift force oscillates periodically.[48] Figure 7 also illustrates the selected initial condition and time window for VIV simulation on the particular time-series data, where the displacement during U_R^* from rest initial condition is zero (only flow past a stationary cylinder on the U_R^*-from-rest initial condition).

A slight fluctuation is observed in the time-series data of cylinder displacement, as presented in Fig. 7. This slight fluctuation is induced by a turbulent wake downstream of the vibrating cylinder. Zhao *et al.*[5] used 3-D direct numerical simulation (DNS) to simulate the VIV of a circular cylinder at Re = 1000 and observed the same slight fluctuation in the time-series data of cylinder displacement. In addition, an experimental study of VIV of a circular cylinder in the turbulent flow regime performed by Govardhan and Williamson[52] showed similar fluctuation in time-series data of displacement.

The Important data that can be exported from time-series data are the frequency domain data. Figures 8 and 9 show the results from FFT and HHT analyses of displacement data from a single-cylinder

case with the following parameters: $m^* = 10.0$, $\zeta = 0.01$, $U_R^* = 6.0$, and $\mathrm{Re} = 1000$. FFT and HHT analyses are applied to the time-series data of cylinder displacement in the predefined time window. In this case, FFT analysis shows the dominant harmonic with frequency $f_s^* = 0.1586$. HHT analysis for this case also indicates an almost constant value of instantaneous frequency in the Hilbert spectrum throughout the time window. There is only a slight disturbance at $t^* = 1100$, and this disturbance is a consequence of the slight fluctuation of time-series data in Fig. 7.

Figure 10 illustrates the instantaneous flow field captured and colored by Q-criterion and spanwise vorticity for single and SBS cylinders ($g^* = 1.5$) cases with the following parameters: $m^* = 10.0$, $\zeta = 0.01$, $U_R^* = 6.0$, and $\mathrm{Re} = 1000$. The turbulent wake structure behind the cylinder, which is similar to the results presented by Zhao *et al.*[5] (Fig. 8), is clearly observed in this study. The vortex-shedding behind the single cylinder forms two single (2S) mode patterns, where two single vortices are released every vibration cycle. The wake pattern behind the SBS cylinders is associated with the response correlation of vibrating SBS cylinders. In this case, the response correlation between SBS cylinders ($g^* = 1.5$) at $U_R^* = 6$ is in-phase, so the wake pattern also becomes in-phase. The vortices merge immediately after being released from each cylinder and then move in pairs together. Section

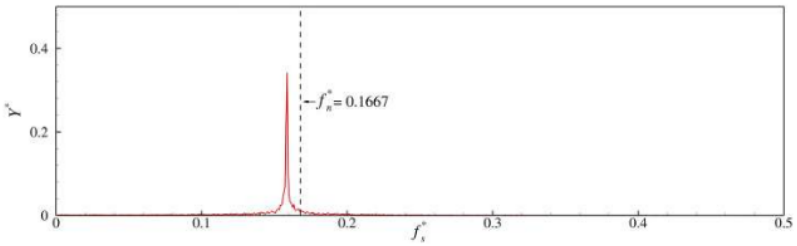

FIG. 8. FFT analysis of displacement data from a single-cylinder case with the following parameters: $m^* = 10.0$, $\zeta = 0.01$, $U_R^* = 6.0$, and $\mathrm{Re} = 1000$.

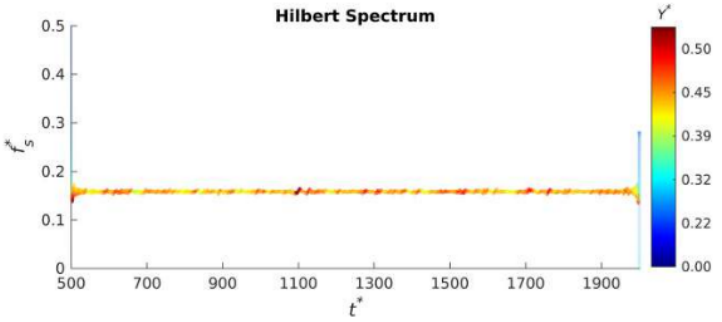

FIG. 9. HHT analysis of displacement data from a single-cylinder case with the following parameters: $m^* = 10.0$, $\zeta = 0.01$, $U_R^* = 6.0$, and $\mathrm{Re} = 1000$.

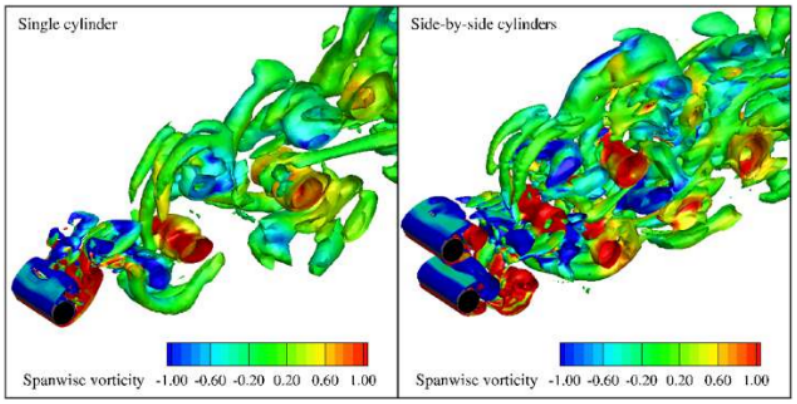

FIG. 10. Instantaneous flow field captured and colored by Q-criterion and spanwise vorticity for single and SBS cylinders ($g^* = 1.5$) cases with the following parameters: $m^* = 10.0$, $\zeta = 0.01$, $U_R^* = 6.0$, and $\mathrm{Re} = 1000$.

III B will present more examples and detail of responses correlation analysis. In addition, the mixing of vortices behind the SBS cylinders changes the vortex-shedding frequency of each cylinder and reduces the vibration amplitude.[27]

B. VIV responses with different gap ratios

Figures 11 and 12 show the amplitude and frequency responses for VIV of SBS cylinders at $U_R^* = 4.0$ and 6.0 for a range of gap ratios between cylinders. At $U_R^* = 4.0$, the SBS cylinders with $g^* = 1.0$–1.2 show a significant increase in the amplitude response, where the amplitude response is much larger. The amplitude responses of SBS cylinders with $g^* \geq 1.3$ are slightly larger than the response from the single cylinder case at $U_R^* = 4.0$. In this situation, the effect of gap flow interference between SBS cylinders decreases slowly. The same pattern also occurs in the frequency response. The frequency ratio from SBS cylinders comes closer to the frequency ratio of a single cylinder as the gap ratio between cylinders increases. The optimal gap ratio for $U_R^* = 4.0$ is in the range of 1.0–1.2. Larger than that, the VIV responses are close to single-cylinder responses. The different responses appear in the VIV of SBS cylinders at $U_R^* = 6.0$. The small gap ratio between cylinders decreases the amplitude and frequency responses for upper and lower cylinders. As the gap ratio increases, the amplitude and frequency responses increase until reaching the response of a single-cylinder case. For the SBS cylinders with a larger gap ratio, the effect of gap flow between cylinders disappears, where the vibration responses of SBS cylinders are close to the responses of a single cylinder. Based on this observation, the same gap ratio gives different responses for different reduced velocities, which means the optimal gap ratio will be different as long as the reduced velocity is altered.

Figure 13 shows the response correlation between upper and lower cylinders for (a) $U_R^* = 4.0$ and (b) $U_R^* = 6.0$. In Fig. 13(a), the perfect anti-phase is observed for SBS cylinders with $g^* = 1.0$–1.2. The perfect anti-phase correlation is identified with the value of $A(t^*) = -1$, and the straight line of the autocorrelation function appears throughout the time window. This perfect anti-phase correlation leads to a significant increase in the amplitude response of SBS cylinders at $U_R^* = 4.0$, as shown in Fig. 11. In Fig. 13(b), the response correlation from SBS cylinders at $U_R^* = 6.0$ is close to one or in the in-phase correlation. All gap ratios produce almost the same response correlations for this reduced velocity. It can be concluded that there is no significant effect of the gap flow interference in the response correlation of SBS cylinders at $U_R^* = 6.0$. The in-phase correlation leads to the lower amplitude response, as shown in Fig. 12. The anti-phase correlation leads to the strong interaction between SBS cylinders and then significantly increases the vibration response. In contrast, the in-phase correlation leads to the weak interaction between SBS cylinders and does not increase or even decrease the amplitude response.

In the VIV of SBS cylinders, the response correlation between upper and lower cylinders is closely related to the wake pattern from both cylinders. In this case, the VIV responses are dominantly induced by vortex shedding behind the SBS cylinders. The instantaneous flow fields behind the SBS cylinders case with different response correlations are analyzed to observe this relation. The instantaneous flow fields from the single cylinder case in the same reduced velocity are presented to investigate the visible change in the wake pattern near the cylinder. Eight instantaneous flow fields are selected within a complete vibration cycle to see the wake pattern as well as the vortex-shedding modes. The instantaneous flow field is rendered using a spanwise vorticity contour in the interval of −1 to 1 to investigate positive and negative spanwise vorticities. The extracted plane is located at the center

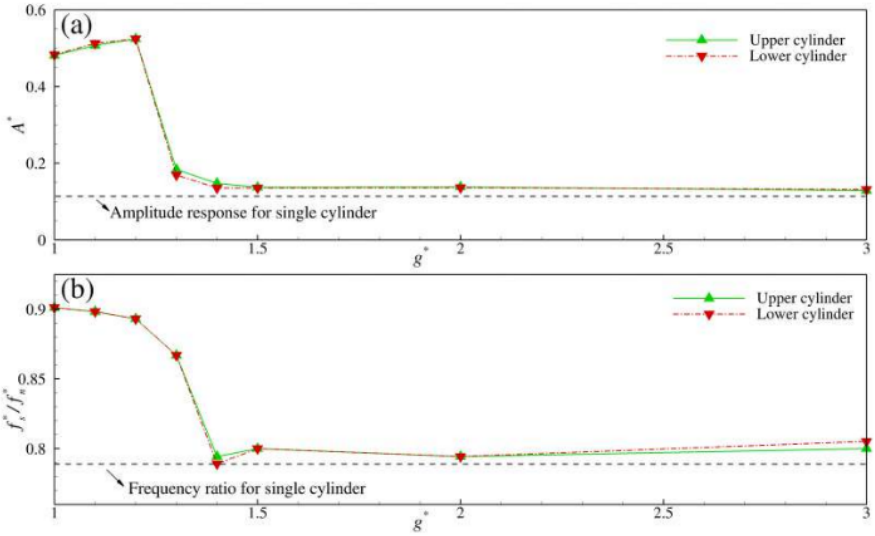

FIG. 11. Results for (a) amplitude response and (b) frequency ratio of two cylinders in the SBS arrangement with different gap ratios ($m^* = 10.0$, $\zeta = 0.01$, $U_R^* = 4.0$, and $\mathrm{Re} = 1000$).

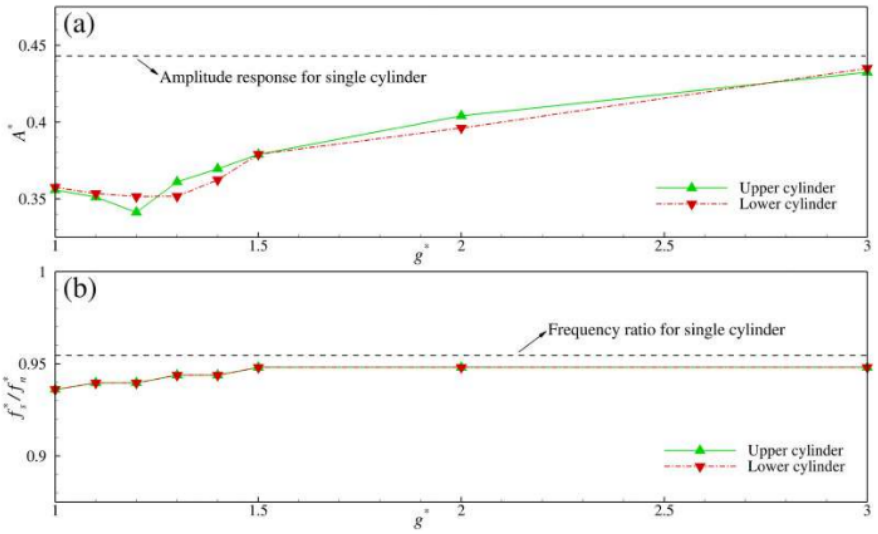

FIG. 12. Results for (a) amplitude response and (b) frequency ratio of two cylinders in the SBS arrangement with different gap ratios ($m^* = 10.0$, $\zeta = 0.01$, $U_R^* = 6.0$, and $\mathrm{Re} = 1000$).

of the z-plane ($z = 1.5$). For the single-cylinder case, a square symbol in red in the time series data represents the position of the selected instantaneous flow field. For the SBS cylinders, square symbols in red and blue represent the position of the instantaneous flow field of lower and upper cylinders, respectively.

Figure 14 reveals the instantaneous spanwise vorticity contour for the single cylinder at $U_R^* = 4.0$. In this figure, two single vortices with reverse circulation are shed from the cylinder during one complete vibration cycle (2S mode). Figures 15 and 16 show the instantaneous spanwise vorticity contours for SBS cylinders with $g^* = 1.2$ and

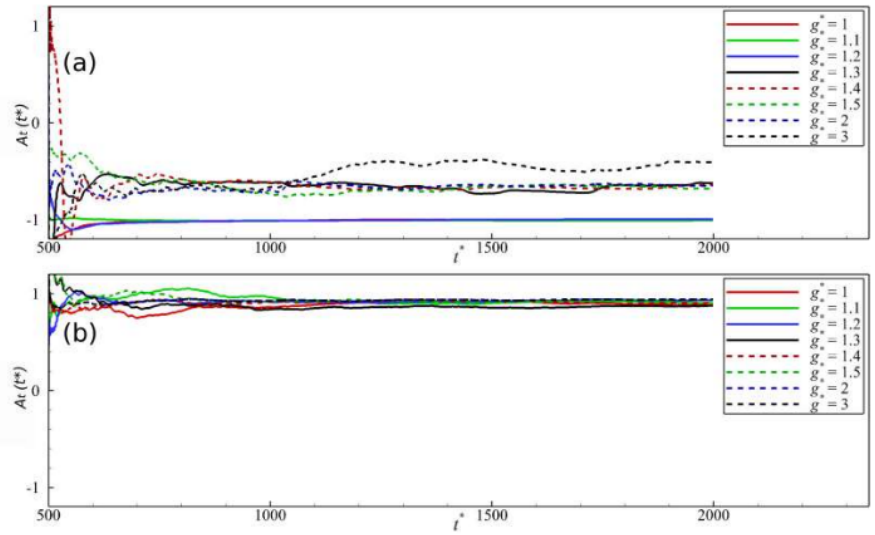

FIG. 13. Response correlation between upper and lower cylinders for (a) $U_R^* = 4.0$ and (b) $U_R^* = 6.0$.

3.0 at $U_R^* = 4.0$. The case of SBS cylinders with $g^* = 3.0$ (see Fig. 16) shows a similar pattern to the case of the single cylinder (Fig. 14). In Fig. 15, it is found that the SBS cylinders with $g^* = 1.2$ show a different pattern. This result is also reflected in the amplitude and frequency responses of SBS cylinders in Fig. 11, where the responses from the SBS case with $g^* = 3.0$ are close to the single-cylinder response. The clear flow field comparison in Figs. 14–16 is presented with the video animation on the following link (https://www.youtube.com/watch?v=5psVjsfoOoY).

The wake pattern behind SBS cylinders with $g^* = 1.2$ (see Fig. 15) shows the anti-phase pattern. The inner vortices released by the two cylinders immediately merge when the upper cylinder moves upward, and the lower cylinder moves downward. When both cylinders move in reverse directions, it seems that the gap between the two cylinders is narrowed. The outer vortices merge a little further away from SBS cylinders. The anti-phase wake pattern leads the SBS cylinders to vibrate in opposite directions. This condition allows a collision between the two cylinders if the gap ratio is small enough. The case of

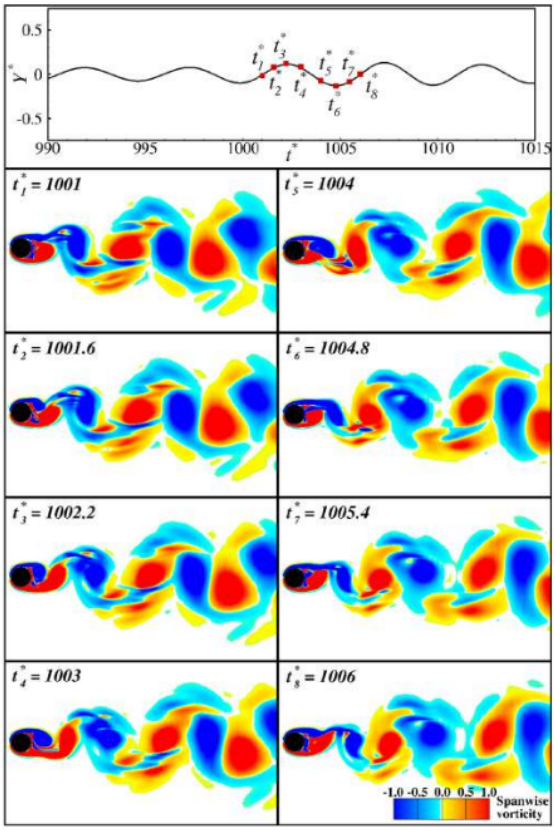

FIG. 14. Instantaneous spanwise vorticity contours for the case of the single cylinder at $U_R^* = 4.0$.

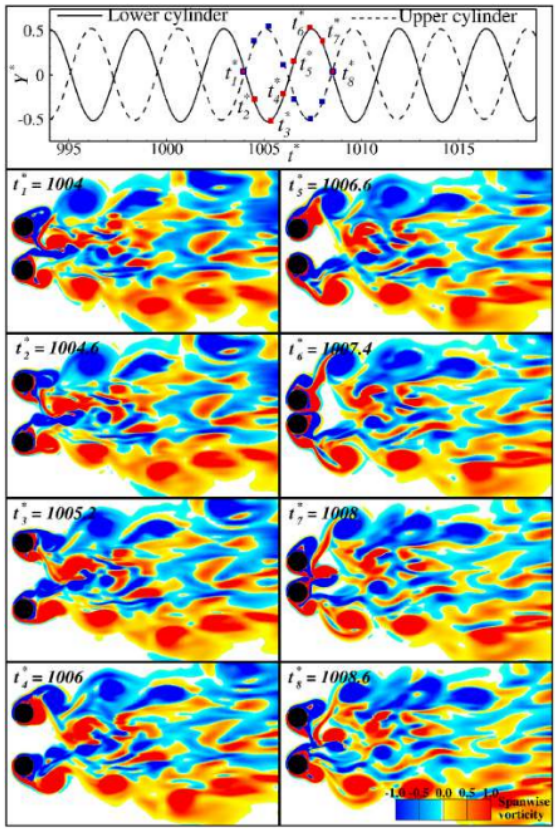

FIG. 15. Instantaneous spanwise vorticity contours for the case of SBS cylinders ($g^* = 1.2$) at $U_R^* = 4.0$.

SBS cylinders with $g^* = 3.0$ (Fig. 16) shows the irregular wake pattern where the vortex coalescence occurs in the far wake region. This finding explains the result in Fig. 13(a), where the autocorrelation function for SBS cylinders with $g^* = 3.0$ is more close to zero. Figure 17 shows the instantaneous spanwise vorticity contours for SBS cylinders ($g^* = 1.2$) at $U_R^* = 6.0$. The in-phase wake pattern is observed, where the inner and outer vortices merge after being released from the SBS cylinders. The in-phase wake pattern leads the SBS cylinders to vibrate in the same direction. This condition keeps the constant gap between cylinders during oscillation. The video animation of the in-phase and anti-phase wake pattern of SBS cylinders is presented in the following link (https://www.youtube.com/watch?v=gtu2J5FnNEU).

The crucial information that should be observed in energy harvesting devices is efficiency. This information usually represents the amount of energy converted from the available potential energy. This present study uses the efficiency formula of the VIVACE converter proposed by Li *et al.*[25,44] and Ding *et al.*[53] [Eq. (20)] to get the VIVACE efficiency of the vibrating cylinder with respect to the gap

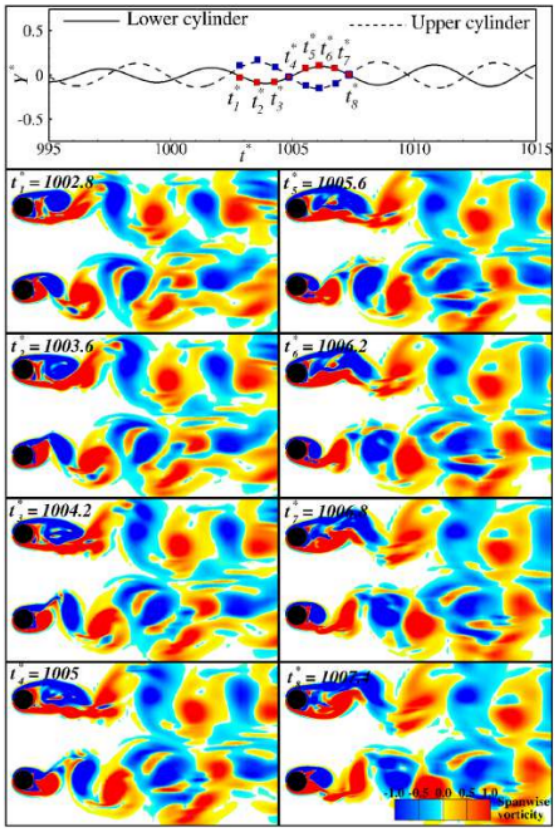

FIG. 16. Instantaneous spanwise vorticity contours for the case of SBS cylinders ($g^* = 3$) at $U_R^* = 4.0$.

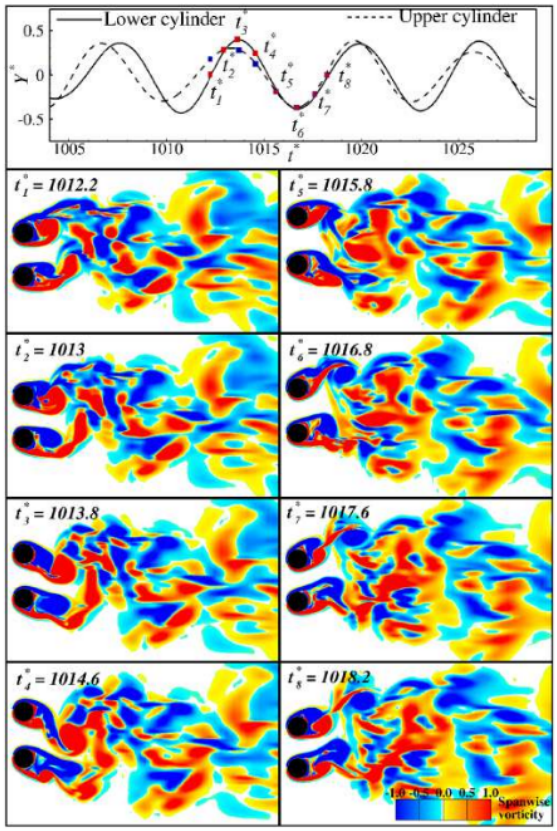

FIG. 17. Instantaneous spanwise vorticity contours for the case of SBS cylinders ($g^* = 1.2$) at $U_R^* = 6.0$.

ratio. Figure 18 shows the VIVACE efficiency for single cylinder and SBS cylinders for the gap ratio at $U_R^* = 4.0$ and $U_R^* = 6.0$. The VIVACE efficiency from SBS cylinders with $g^* = 3.0$ is close to the one of the single-cylinder. Therefore, the effect of the SBS arrangement is minimal at this gap ratio. At $U_R^* = 4.0$, the SBS cylinders with the gap ratio $g^* = 1.0$–1.2 show a significant increase in the VIVACE efficiency. The SBS cylinders with $g^* = 1.2$ produce the highest efficiency in this reduced velocity. That is, the optimal gap ratio for this reduced velocity is $g^* = 1.2$. At $U_R^* = 6.0$, the VIVACE efficiency is less than the single-cylinder case. In this case, the smaller gap ratio reduces the VIVACE efficiency. The larger gap ratio leads to the same efficiency as the single cylinder. The VIVACE efficiency of the single cylinder is $\eta_{V\,IV\,ACE} = 0.0051$ at $U_R^* = 4.0$. For the SBS cylinders with $g^* = 1.2$, the efficiency is $\eta_{V\,IV\,ACE} = 0.1332$ at $U_R^* = 4.0$. Based on Figs. 13 and 18, the anti-phase correlation between SBS cylinders leads to higher efficiency. However, the in-phase correlation between SBS cylinders reduces the efficiency in comparison with the single-cylinder case.

C. Amplitude response and VIVACE efficiency with different VIV parameters and flow conditions

Figure 19 shows a comparison of the amplitude response of two vibrating SBS cylinders with different VIV parameters and flow conditions. Chen *et al.*[27] investigated the VIV responses of SBS cylinders ($g^* = 1.0$) at $\mathrm{Re} = 500$ with the following VIV parameters: $m^* = 2.0$, $\zeta = 0.0$, and $U_R^* = 2.0$ to 10.0. Due to the differences in the VIV parameters and the flow conditions, the amplitude response of this current study and the published result from Chen *et al.*[27] are generally different from one another. In the present investigation, $m^* = 4.0$, $\zeta = 0.025$, and $\mathrm{Re} = 1000$ are used. In addition, the gap ratio is slightly larger, specifically $g^* = 1.2$. Even though the simulation parameters are different, some behaviors of the vibrating SBS cylinders are similar in both cases. The amplitude response in the upper and lower cylinders is almost identical in both cases. For $U_R^* \leq 4.0$, the amplitude response of vibrating SBS cylinders will increase as U_R^* increases. The maximum amplitude response from both cases is also observed at

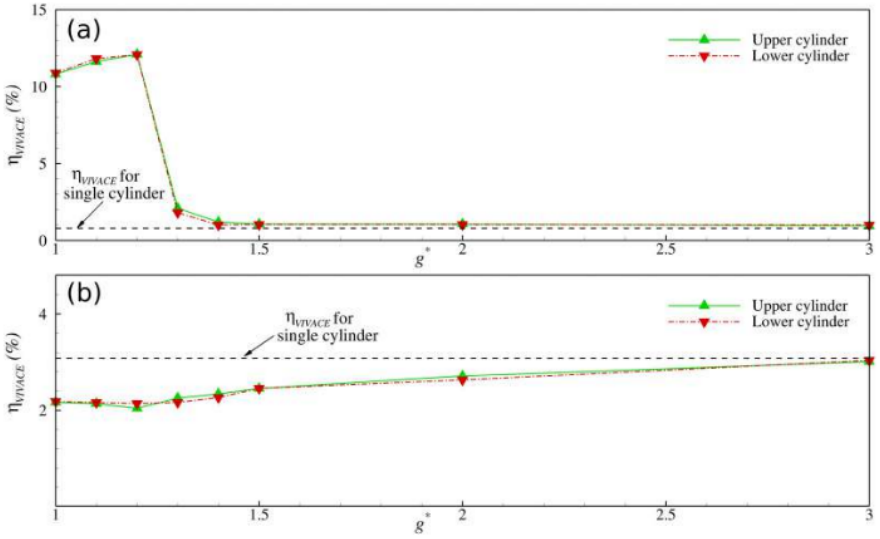

FIG. 18. VIVACE efficiencies of a single cylinder and SBS cylinders at (a) $U_R^* = 4.0$ and (b) $U_R^* = 6.0$.

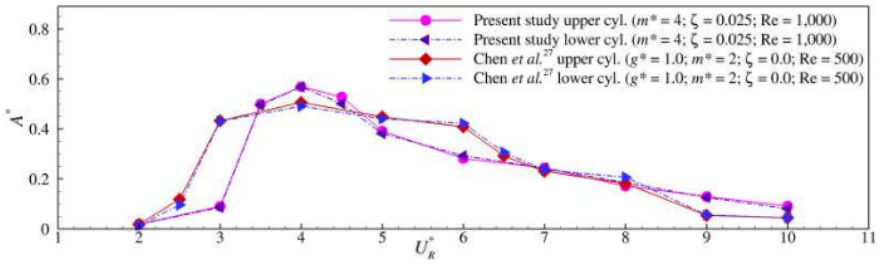

FIG. 19. Amplitude response of the vibrating SBS cylinders. The published result from Chen *et al.*[27] is attached for comparison.

$U_R^* = 4.0$. When $U_R^* > 4.0$, the amplitude response of both upper and lower cylinders will gradually decrease as U_R^* increases. In terms of these results, it turns out that the present numerical solver has been proven to predict the VIV response of vibrating SBS cylinders for the selected range of U_R^*.

In order to investigate the effect of VIV parameters and flow conditions on the amplitude response and VIVACE efficiency, each parameter will be altered while the other parameters remain unchanged. The amplitude response and VIVACE efficiency will be observed in the same U_R^* range. Figure 20 shows the amplitude response and VIVACE efficiency of vibrating SBS cylinders with different damping ratios at Re = 1000. The vibrating SBS cylinders with a smaller damping ratio tend to produce a larger amplitude response. Only at $U_R^* = 5.0$, the amplitude response is slightly smaller than that with a larger damping ratio. When the cylinder vibrates, a lower damping ratio results in less resistance, which allows for the cylinder to achieve a greater amplitude. When the amplitude response increases drastically, the VIVACE efficiency will also increase significantly. In this case, the SBS cylinders with $\zeta = 0.01$ produce a significant amplitude and efficiency at $U_R^* = 4.0$. However, for the SBS cylinders with $\zeta = 0.025$, the significant amplitude and efficiency start to appear at $U_R^* = 4.5$. According to Eq. (20), the VIVACE efficiency is inherently linked to the value of the damping ratio. In the VIVACE system, the converted energy is the amount of energy dissipated by the damper. With nearly identical amplitude responses ($U_R^* = 4.5$–5.0), the SBS cylinders with a lower damping ratio dissipate less energy, resulting in poorer efficiencies than those with a larger damping ratio, as shown in Fig. 20(b). The SBS cylinders with a larger damping ratio result in a higher maximum efficiency with a narrower U_R^* range for significant efficiency. Similar results were also observed by Barrero-Gil *et al.*[26] when analyzing the energy conversion efficiency of an elastically mounted single cylinder, where a single vibrating cylinder with a

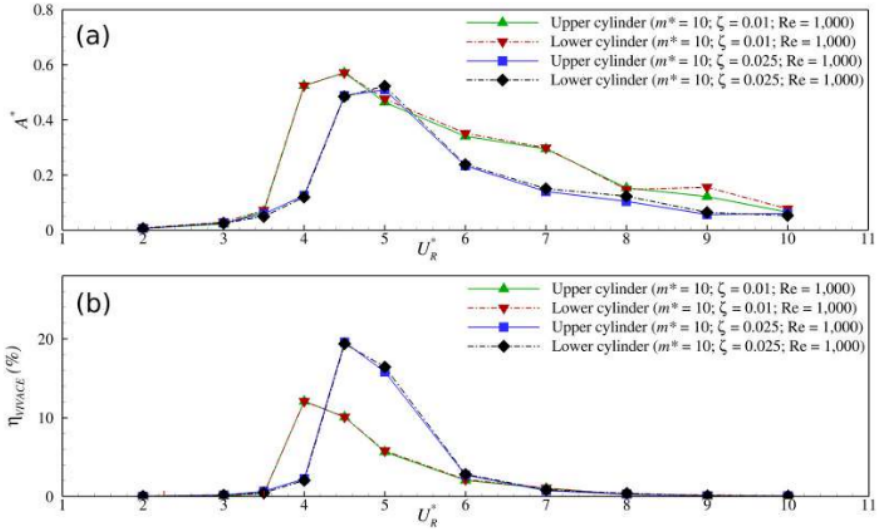

FIG. 20. Results for (a) amplitude response and (b) VIVACE efficiency of vibrating SBS cylinders with different damping ratios at Re = 1000.

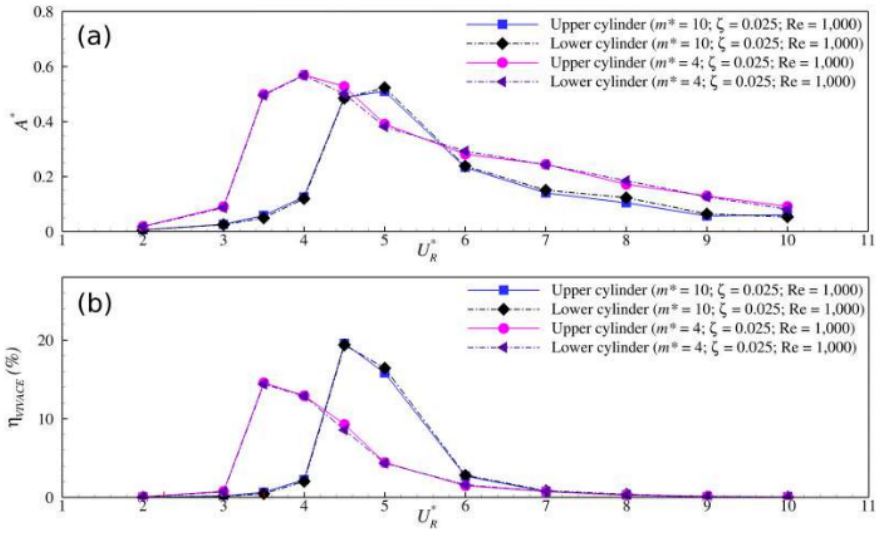

FIG. 21. Results for (a) amplitude response and (b) VIVACE efficiency of vibrating SBS cylinders with different mass ratios at Re = 1000.

higher damping ratio resulted in a higher maximum efficiency with a narrower U_R^* range for significant efficiency. The results from experiments with a single cylinder of VIVACE by Sun *et al.*[43] and Li *et al.*[44] also demonstrated that the harvesting energy system performed better with a higher damping ratio.

Figure 21 shows the amplitude response and VIVACE efficiency of the vibrating SBS cylinders with different mass ratios at Re = 1000. The case of SBS cylinders with a smaller mass ratio tends to produce a larger amplitude response, except at $U_R^* = 5.0$. With the same damping ratio, the case of SBS cylinders with a small mass ratio shows a wider

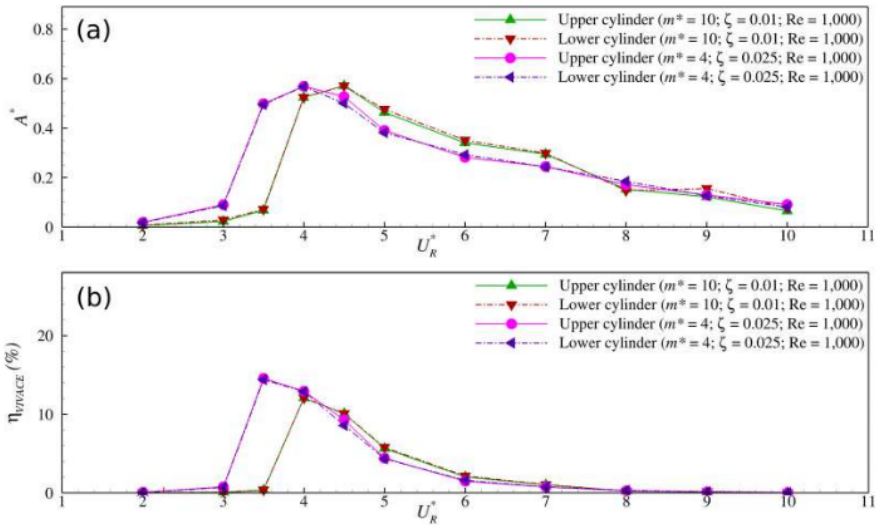

FIG. 22. Results for (a) amplitude response and (b) VIVACE efficiency of vibrating SBS cylinders with $m^*\zeta = 0.1$ at Re = 1000.

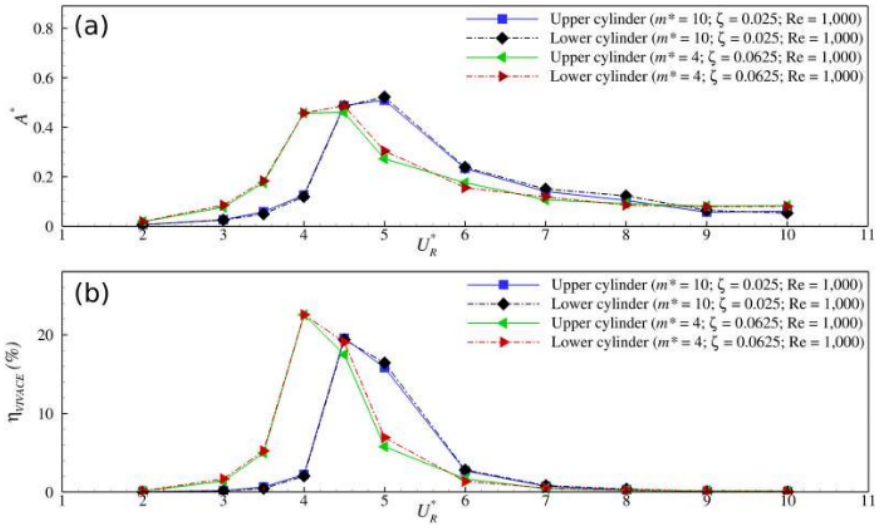

FIG. 23. Results for (a) amplitude response and (b) VIVACE efficiency of vibrating SBS cylinders with $m^*\zeta = 0.25$ at Re = 1000.

U_R^* range of significant amplitude response. The SBS cylinders with $m^* = 4.0$ start to produce high amplitudes at $U_R^* = 3.5$, while the SBS cylinders with $m^* = 10.0$ produce high amplitudes starting from $U_R^* = 4.5$. A similar pattern was also observed by Barrero-Gil *et al.*[26] for a single vibrating cylinder with different mass ratios. Similar to the damping ratio, the mass ratio is also directly related to the efficiency of the VIVACE system. As explained in Eqs. (18) and (20), in the VIVACE efficiency calculation, the mass ratio is at the numerator position. So with almost the same amplitude response, the SBS cylinders with a low mass ratio will result in lower VIVACE efficiency. In

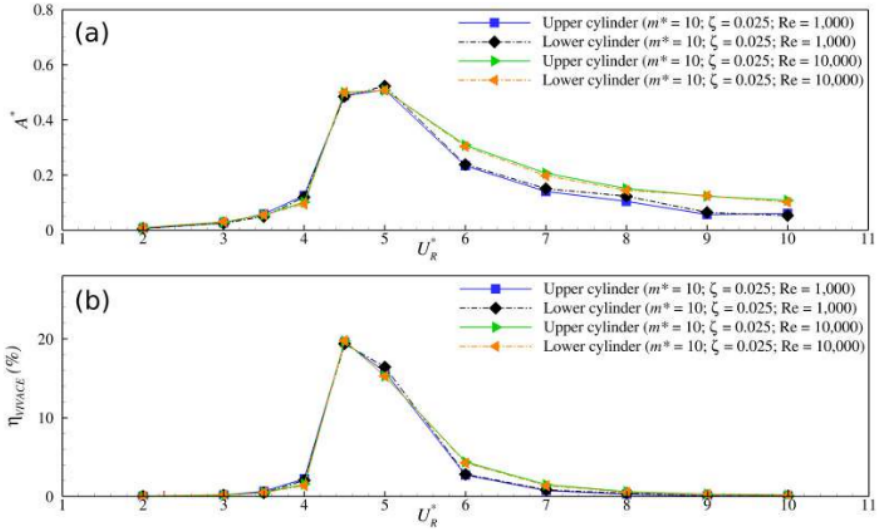

FIG. 24. Results for (a) amplitude response and (b) VIVACE efficiency of vibrating SBS cylinders with $m^*\zeta = 0.25$ at different flow conditions.

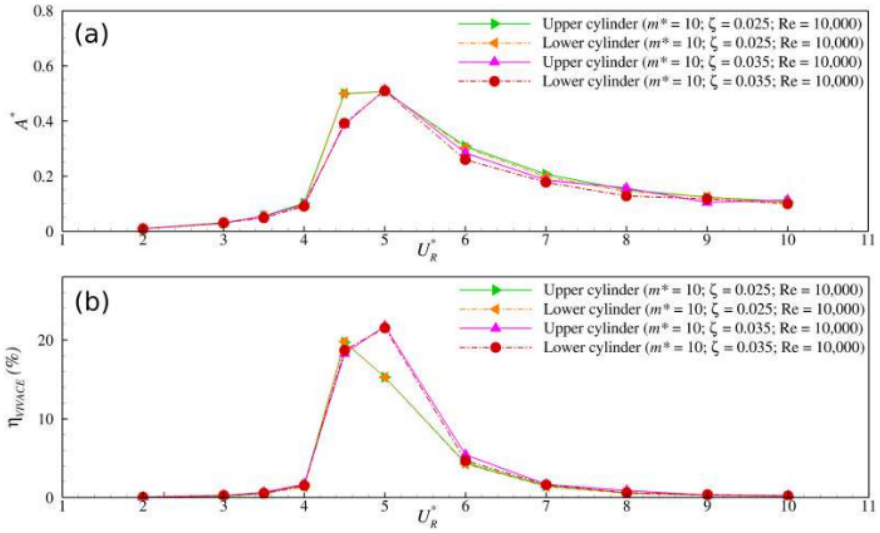

FIG. 25. Results for (a) amplitude response and (b) VIVACE efficiency of vibrating SBS cylinders with different damping ratios at Re = 10 000.

Fig. 21, the amplitude responses of SBS cylinders with $m^* = 4.0$ show a significant increase at $U_R^* = 3.5$–4.0, so the VIVACE efficiency at these U_R^* also increases significantly. In the other U_R^*, the difference in amplitude response of the two cases is insignificant, so the VIVACE efficiency of SBS cylinders with the higher mass ratio is better, as shown in Fig. 21(b).

Barrero-Gil *et al.*[26] found that the energy extraction process from the VIV of a single cylinder at the constant Re is affected by the mass-damping parameter $m^*\zeta$. The combination of mass ratio and damping ratio with the same mass-damping parameters produces almost similar maximum values of amplitude response and VIVACE efficiency. Figure 22 shows the amplitude response and VIVACE efficiency of

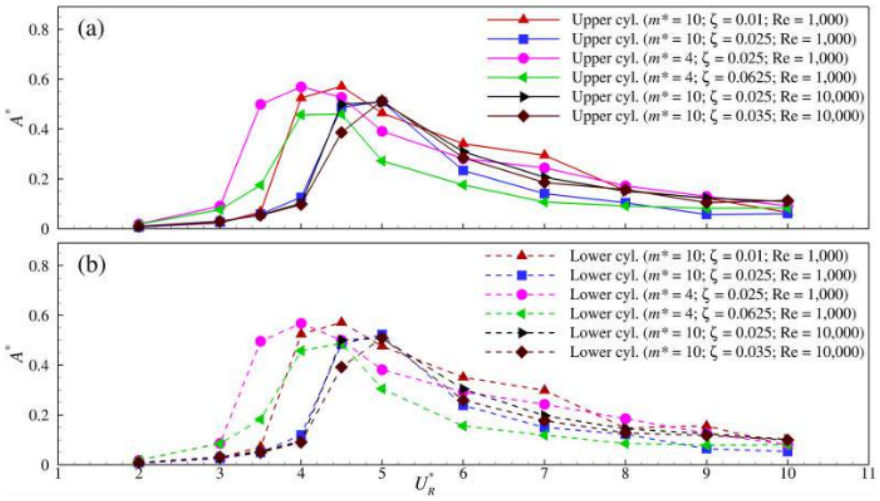

FIG. 26. Amplitude response for (a) upper cylinder and (b) lower cylinder of vibrating SBS cylinders with different parameters.

vibrating SBS cylinders with $m^*\zeta = 0.1$ at Re = 1000. The maximum amplitude response of both SBS cases is almost the same. The only difference is the starting point of the significant amplitude. With the same $m^*\zeta$, SBS cylinders with $m^* = 4.0$ result in a significant amplitude response starting from $U_R^* = 3.5$, while for SBS cylinders with $m^* = 10.0$, a high amplitude response begins at $U_R^* = 4.0$. Based on Fig. 22(a), the maximum amplitude response for both cases is almost similar ($A^* \approx 0.57$). The only difference is the value of U_R^* with maximum amplitude. In this case, the pattern of significant amplitude response from SBS cylinders with lower m^* shifts to the lower U_R^* region. A slightly different pattern is observed in the VIVACE efficiency, where SBS cylinders with a lower m^* result in slightly better maximum efficiency, as shown in Fig. 22(b). In addition, the U_R^* range for significant efficiency is also slightly wider. Figure 23 shows the amplitude response and VIVACE efficiency of vibrating SBS cylinders with $m^*\zeta = 0.25$ at Re = 1000. Almost the same pattern is also observed in Fig. 23, where the maximum amplitude of two SBS cases is nearly the same, and the maximum VIVACE efficiency of SBS cylinders with smaller m^* is slightly better. In addition, a significant shift in the amplitude and efficiency response patterns is also clearly observed

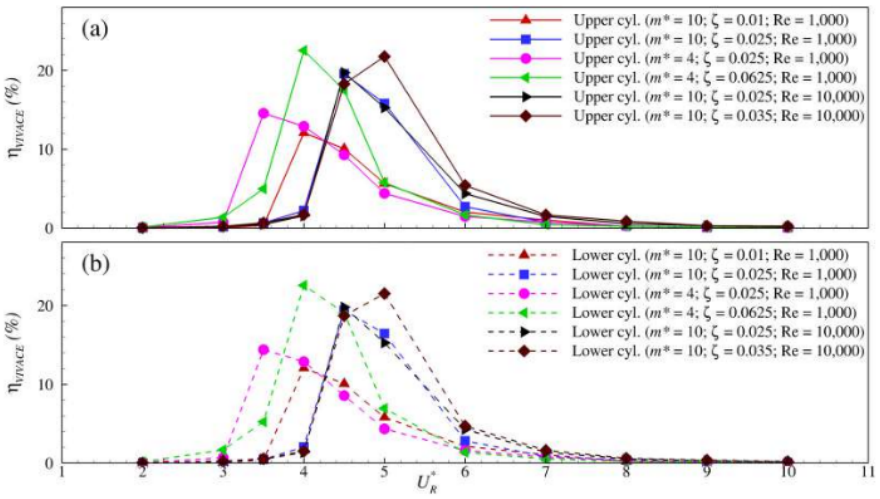

FIG. 27. VIVACE efficiency for (a) upper cylinder and (b) lower cylinder of vibrating SBS cylinders with different parameters.

in Fig. 23. These results indicate that the effect of $m^*\zeta$ on vibrating SBS cylinders is slightly different from that of a single vibrating cylinder. This difference is caused by the gap flow between vibrating SBS cylinders, which results in disturbance so that the VIV response is different from that of a single cylinder.[27,31] Based on the supplied data, it appears that a low m^* could be desirable in order to increase the U_R^* range of significant VIVACE efficiency and pick the right ζ to reach a high value of maximum VIVACE efficiency. The reason for this is that a broader range of effective VIVACE operations is possible with a low m^*.

Figure 24 shows the amplitude response and VIVACE efficiency of vibrating SBS cylinders with different flow conditions. Here, the same VIV parameters ($m^* = 10.0$ and $\zeta = 0.025$) are used for both SBS cases with different flow conditions. The amplitude response from both SBS cases is almost identical, and only at $U_R^* \geq 6.0$, the amplitude responses from the SBS case with $\mathrm{Re} = 10\,000$ are slightly larger than the SBS case with $\mathrm{Re} = 1000$. Even so, the resulting response pattern also remains the same. An identical result is observed for the VIVACE efficiency of SBS cylinders with different Re, as shown in Fig. 24(b). Based on these results, it can be concluded that the effect of flow conditions on the amplitude response and VIVACE efficiency of vibrating SBS cylinders with the same VIV parameters is not significant. Figure 25 shows the amplitude response and VIVACE efficiency of vibrating SBS cylinders with different damping ratios at $\mathrm{Re} = 10\,000$. For this case, the effect of the damping ratio looks similar to the previous case with a lower Re (Fig. 20), where the vibrating SBS cylinders with a larger damping ratio produce higher maximum VIVACE efficiency. In addition, the value of U_R^* with maximum efficiency also shifts to the right (toward a higher U_R^*) when the damping ratio increases. From the results, it appears that the effect of VIV parameters looks similar under different flow conditions.

Figures 26 and 27 present the amplitude response and VIVACE efficiency for upper and lower cylinders with different parameters. A previous study conducted by Chen *et al.*[18] investigated the 1-DoF (degree of freedom) VIV of vibrating SBS cylinders at $\mathrm{Re} = 60$–200. It was found that the amplitude response of vibrating SBS cylinders is almost identical. A similar result was observed by Chen *et al.*[27] for the 1-DoF VIV case of vibrating SBS cylinders at $\mathrm{Re} = 500$. As presented in Fig. 26, the amplitude responses from upper and lower cylinders are almost identical as well. There is no significant difference between the amplitude responses of upper and lower cylinders for different VIV parameters. At $\mathrm{Re} = 1000$, two cases with $m^* = 10$; $\zeta = 0.01$ and $m^* = 4.0$; and $\zeta = 0.025$ show better amplitude responses with a wider U_R^* range for the significant amplitude. At $\mathrm{Re} = 10\,000$, the case with $m^* = 10$; $\zeta = 0.025$ shows a slightly better amplitude result, especially at $U_R^* = 4.5$. Based on these results, it can be concluded that the amplitude response from vibrating SBS cylinders is identical up to $\mathrm{Re} = 10\,000$. As presented in Fig. 27, a similar pattern is found in the response of VIVACE efficiency, where the results from upper and lower cylinders are almost identical. The case with $m^* = 4.0$ and $\zeta = 0.0625$ produces the maximum VIVACE efficiency at $U_R^* = 4.0$ for $\mathrm{Re} = 1000$. For $\mathrm{Re} = 10\,000$, the case with $m^* = 10$ and $\zeta = 0.035$ produces the maximum VIVACE efficiency at $U_R^* = 5.0$.

IV. CONCLUSIONS

The 3-D numerical simulation for VIV of an elastically mounted cylinder in the SBS arrangement was performed using the DFIB-LES techniques. Both vibrating cylinders were allowed to vibrate freely in the transverse direction. The numerical investigation was divided into two parts. The first numerical investigation studied the VIV responses and VIVACE efficiency of vibrating SBS cylinders with varying gap ratios, $g^* = 1.0$–3.0. The VIV parameters and flow condition for this investigation were $U_R^* = 4.0$ and 6.0, $m^* = 10.0$, $\zeta = 0.01$, and $\mathrm{Re} = 1000$. The second numerical investigation studied the influence of VIV parameters and flow conditions in the amplitude response and VIVACE efficiency of SBS cylinders for a range of reduced velocities. This investigation is performed in the range of $2.0 \leq U_R^* \leq 10.0$ with following parameters: $g^* = 1.2$; $m^* = 4.0$ and 10.0; $\zeta = 0.01$, 0.025, 0.035, and 0.0625; and $\mathrm{Re} = 1000$ and 10 000.

The first numerical investigation showed that the optimal gap ratio for $U_R^* = 4.0$ is in the range of $1.0 \leq g^* \leq 1.2$. Larger than that, the VIV responses are close to single-cylinder responses. At $U_R^* = 6.0$, all gap ratios show lower responses compared with a single-cylinder case. The anti-phase correlation between vibrating SBS cylinders leads to higher VIVACE efficiency. The same gap ratio gives different responses for different reduced velocities. The influence of the gap ratio may be investigated to find the optimal gap ratio in the selected range of reduced velocities. For the second numerical investigation, it was found that the vibrating SBS cylinders with a larger ζ result in higher maximum VIVACE efficiency with a narrower U_R^* range for significant efficiency. With almost the same amplitude response, the SBS cylinders with a lower m^* will result in lower VIVACE efficiency. By using the same $m^*\zeta$ parameters, it appears that a low m^* could be desirable in order to increase the U_R^* range of significant VIVACE efficiency and pick the right ζ to reach a high value of maximum VIVACE efficiency. The reason for this is that a broader range of effective VIVACE operations is possible with a low m^*. Based on the result of VIVACE efficiency, the optimum mass and damping ratios for vibrating SBS cylinders at $\mathrm{Re} = 1000$ are $m^* = 4.0$ and $\zeta = 0.0625$. At $\mathrm{Re} = 10\,000$, the optimum mass and damping ratios are $m^* = 10$ and $\zeta = 0.035$. The effect of flow conditions on the amplitude response and VIVACE efficiency of vibrating SBS cylinders with the same VIV parameters is not significant. In this study, vibrating SBS cylinders are simulated at $\mathrm{Re} = 1000$ and $\mathrm{Re} = 10\,000$. In the future, it would be necessary to perform an investigation for a range of Re to uncover the influence of Re in the amplitude response and VIVACE efficiency of vibrating SBS cylinders.

ACKNOWLEDGMENTS

The authors express their gratitude for the financial support from the Ministry of Science and Technology, Taiwan (Grant No. MOST-111-2221-E-011-083) and the National Center for High-performance Computing (NCHC), Taiwan, for providing computational and storage resources.

AUTHOR DECLARATIONS

Conflict of Interest

The authors have no conflicts to disclose.

Author Contributions

Yosua Heru Irawan: Formal analysis (lead); Methodology (lead); Software (lead); Validation (lead); Visualization (lead); Writing – original draft (lead). **Syed Ahmad Raza:** Methodology (lead); Software

(lead); Validation (lead); Writing – review & editing (lead). **Ming-Jyh Chern:** Conceptualization (lead); Funding acquisition (lead); Project administration (lead); Supervision (lead).

DATA AVAILABILITY

The data that support the findings of this study are available from the corresponding author upon reasonable request.

REFERENCES

[1]P. Anagnostopoulos and P. W. Bearman, "Response characteristics of a vortex-excited cylinder at low Reynolds numbers," J. Fluids Struct. **6**, 39–50 (1992).
[2]T. Nomura, "Finite element analysis of vortex-induced vibrations of bluff cylinders," J. Wind Eng. Ind. Aerodyn. **46–47**, 587–594 (1993).
[3]A. Khalak and C. H. Williamson, "Motions, forces and mode transitions in vortex-induced vibrations at low mass-damping," J. Fluids Struct. **13**, 813–851 (1999).
[4]D. Lucor, J. Foo, and G. E. Karniadakis, "Vortex mode selection of a rigid cylinder subject to VIV at low mass-damping," J. Fluids Struct. **20**, 483–503 (2005).
[5]M. Zhao, L. Cheng, H. An, and L. Lu, "Three-dimensional numerical simulation of vortex-induced vibration of an elastically mounted rigid circular cylinder in steady current," J. Fluids Struct. **50**, 292–311 (2014).
[6]C. H. Williamson and R. Govardhan, "A brief review of recent results in vortex-induced vibrations," J. Wind Eng. Ind. Aerodyn. **96**, 713–735 (2008).
[7]S. Mittal and V. Kumar, "Finite element study of vortex-induced cross-flow and in-line oscillations of a circular cylinder at low Reynolds numbers," Int. J. Numer. Methods Fluids **31**, 1087–1120 (1999).
[8]T. K. Prasanth and S. Mittal, "Vortex-induced vibrations of a circular cylinder at low Reynolds numbers," J. Fluid Mech. **594**, 463–491 (2008).
[9]Navrose and S. Mittal, "Free vibrations of a cylinder: 3-D computations at Re = 1000," J. Fluids Struct. **41**, 109–118 (2013).
[10]M. M. Bernitsas, K. Raghavan, Y. Ben-Simon, and E. M. Garcia, "VIVACE (Vortex Induced Vibration Aquatic Clean Energy): A new concept in generation of clean and renewable energy from fluid flow," J. Offshore Mech. Arct. Eng. **130**, 041101 (2008).
[11]M. M. Zdravkovich and D. L. Pridden, "Interference between two circular cylinders; Series of unexpected discontinuities," J. Wind Eng. Ind. Aerodyn. **2**, 255–270 (1977).
[12]D. Sumner, "Two circular cylinders in cross-flow: A review," J. Fluids Struct. **26**, 849–899 (2010).
[13]Y. Zhou and M. Alam, "Wake of two interacting circular cylinders: A review," Int. J. Heat Fluid Flow **62**, 510–537 (2016).
[14]S. Kang, "Characteristics of flow over two circular cylinders in a side-by-side arrangement at low Reynolds numbers," Phys. Fluids **15**, 2486–2498 (2003).
[15]W. Chen, C. Ji, W. Xu, S. Liu, and J. Campbell, "Response and wake patterns of two side-by-side elastically supported circular cylinders in uniform laminar cross-flow," J. Fluids Struct. **55**, 218–236 (2015).
[16]W. Chen, C. Ji, R. Wang, D. Xu, and J. Campbell, "Flow-induced vibrations of two side-by-side circular cylinders: Asymmetric vibration, symmetry hysteresis and near-wake patterns," Ocean Eng. **110**, 244–257 (2015).
[17]W. Chen, C. Ji, D. Xu, and N. Srinil, "Wake patterns of freely vibrating side-by-side circular cylinders in laminar flows," J. Fluids Struct. **89**, 82–95 (2019).
[18]W. Chen, C. Ji, D. Xu, H. An, and Z. Zhang, "Flow-induced vibrations of two side-by-side circular cylinders at low Reynolds numbers," Phys. Fluids **32**, 023601–5129013 (2020).
[19]B. Liu and R. K. Jaiman, "Dynamics and stability of gap-flow interference in a vibrating side-by-side arrangement of two circular cylinders," J. Fluid Mech. **855**, 804–838 (2018).
[20]A. Munir, M. Zhao, H. Wu, and L. Lu, "Effects of gap ratio on flow-induced vibration of two rigidly coupled side-by-side cylinders," J. Fluids Struct. **91**, 102726 (2019).
[21]Y. Lv, L. Sun, M. M. Bernitsas, M. Jiang, and H. Sun, "Modelling of a flow-induced oscillation, two-cylinder, hydrokinetic energy converter based on experimental data," Energies **14**, 827 (2021).
[22]W. Ding, H. Sun, W. Xu, and M. M. Bernitsas, "Experimental and computational investigation of interactive flow induced oscillations of two tandem rough cylinders at $3 \times 10^4 \leq \mathrm{Re} \leq 1.2 \times 10^5$," Ocean Eng. **223**, 108641 (2021).
[23]C. M. Lee, K. J. Paik, E. S. Kim, and I. Lee, "A fluid-structure interaction simulation on the wake-induced vibration of tandem cylinders with pivoted rotational motion," Phys. Fluids **33**, 045107 (2021).
[24]W. Yuan, H. Sun, E. S. Kim, H. Li, N. Beltsos, and M. M. Bernitsas, "Hydrokinetic energy conversion by flow-induced oscillation of two tandem cylinders of different stiffness," J. Offshore Mech. Arct. Eng. **143**, 062001 (2021).
[25]M. Li, C. C. Bernitsas, J. Guo, and H. Sun, "Synergistic flow-induced oscillation of multiple cylinders in harvesting marine hydrokinetic energy," J. Offshore Mech. Arct. Eng. **143**, 032003 (2021).
[26]A. Barrero-Gil, S. Pindado, and S. Avila, "Extracting energy from vortex-induced vibrations: A parametric study," Appl. Math. Modell. **36**, 3153–3160 (2012).
[27]W. Chen, C. Ji, D. Xu, and M. M. Alam, "Three-dimensional direct numerical simulations of two interfering side-by-side circular cylinders at intermediate spacing ratios," Appl. Ocean Res. **123**, 103162 (2022).
[28]S. A. Raza, M. J. Chern, H. Susanto, and Y. H. Zhou, "Numerical investigation of the effects of a small fixed sphere in tandem arrangement on VIV of a sphere," J. Wind Eng. Ind. Aerodyn. **206**, 104368 (2020).
[29]S. A. Raza, Y. H. Irawan, and M.-J. Chern, "Effect of boundary conditions and domain size on the turbulent flow characteristics over a circular cylinder," J. Chin. Inst. Eng. **44**, 659–672 (2021).
[30]S. Ahmad, Y. Heru, and M.-J. Chern, "Effect of grid size and initial conditions on vortex-induced vibration of a circular cylinder," Ocean Eng. **263**, 112332 (2022).
[31]Y. H. Irawan, S. A. Raza, and M.-J. Chern, "Numerical predictions of vibration responses and flow energy conversion efficiency of side-by-side cylinders at moderate Reynolds number," Appl. Ocean Res. **129**, 103392 (2022).
[32]D. Z. Noor, M. J. Chern, and T. L. Horng, "An immersed boundary method to solve fluid-solid interaction problems," Comput. Mech. **44**, 447–453 (2009).
[33]M. J. Chern, Y. H. Kuan, G. Nugroho, G. T. Lu, and T. L. Horng, "Direct-forcing immersed boundary modeling of vortex-induced vibration of a circular cylinder," J. Wind Eng. Ind. Aerodyn. **134**, 109–121 (2014).
[34]M. J. Chern, D. Z. Noor, C. B. Liao, and T. L. Horng, "Direct-forcing immersed boundary method for mixed heat transfer," Commun. Comput. Phys. **18**, 1072–1094 (2015).
[35]M. J. Chern, G. T. Lu, Y. H. Kuan, S. Chakraborty, G. Nugroho, C. B. Liao, and T. L. Horng, "Numerical study of vortex-induced vibration of circular cylinder adjacent to plane boundary using direct-forcing immersed boundary method," J. Mech. **34**, 177–191 (2018).
[36]T. K. Prasanth, S. Behara, S. P. Singh, R. Kumar, and S. Mittal, "Effect of blockage on vortex-induced vibrations at low Reynolds numbers," J. Fluids Struct. **22**, 865–876 (2006).
[37]T. K. Prasanth, V. Premchandran, and S. Mittal, "Hysteresis in vortex-induced vibrations: Critical blockage and effect of $m*$," J. Fluid Mech. **671**, 207–225 (2011).
[38]N. Kondo, "Three-dimensional computation for flow-induced vibrations of an upstream circular cylinder in two tandem circular cylinders," Int. J. Comput. Fluid Dyn. **28**, 461–476 (2014).
[39]D. Pastrana, J. C. Cajas, O. Lehmkuhl, I. Rodríguez, and G. Houzeaux, "Large-eddy simulations of the vortex-induced vibration of a low mass ratio two-degree-of-freedom circular cylinder at subcritical Reynolds numbers," Comput. Fluids **173**, 118–132 (2018).
[40]E. Wang, Q. Xiao, and A. Incecik, "Three-dimensional numerical simulation of two-degree-of-freedom VIV of a circular cylinder with varying natural frequency ratios at Re = 500," J. Fluids Struct. **73**, 162–182 (2017).
[41]M. J. Chern, P. Rajesh Kanna, Y. J. Lu, I. C. Cheng, and S. C. Chang, "A CFD study of the interaction of oscillatory flows with a pair of side-by-side cylinders," J. Fluids Struct. **26**, 626–643 (2010).
[42]M. J. Chern, F. R. Purnadiana, D. Z. Noor, T. L. Horng, S. W. Chau, and E. Odhiambo, "Numerical study of flow past two counter rotating cylinders using immersed boundary method," J. Mar. Sci. Technol. (Taiwan) **23**, 761–773 (2015).
[43]H. Sun, E. S. Kim, G. Nowakowski, E. Mauer, and M. M. Bernitsas, "Effect of mass-ratio, damping, and stiffness on optimal hydrokinetic energy conversion of a single, rough cylinder in flow induced motions," Renewable Energy **99**, 936–959 (2016).

[44]N. Li, H. Park, H. Sun, and M. M. Bernitsas, "Hydrokinetic energy conversion using flow induced oscillations of single-cylinder with large passive turbulence control," Appl. Energy **308**, 118380 (2022).
[45]M. M. Tavakol, O. Abouali, and M. Yaghoubi, "Large eddy simulation of turbulent flow around a wall mounted hemisphere," Appl. Math. Modell. **39**, 3596–3618 (2015).
[46]I. B. Celik, Z. N. Cehreli, and I. Yavuz, "Index of resolution quality for large eddy simulations," J. Fluids Eng. **127**, 949–958 (2005).
[47]A. Khalak and C. H. Williamson, "Fluid forces and dynamics of a hydroelastic structure with very low mass and damping," J. Fluids Struct. **11**, 973–982 (1997).
[48]E. Guilmineau and P. Queutey, "Numerical simulation of vortex-induced vibration of a circular cylinder with low mass-damping in a turbulent flow," J. Fluids Struct. **19**, 449–466 (2004).
[49]Z. Y. Pan, W. C. Cui, and Q. M. Miao, "Numerical simulation of vortex-induced vibration of a circular cylinder at low mass-damping using RANS code," J. Fluids Struct. **23**, 23–37 (2007).
[50]N. B. Khan, Z. Ibrahim, M. I. Khan, T. Hayat, and M. F. Javed, "VIV study of an elastically mounted cylinder having low mass-damping ratio using RANS model," Int. J. Heat Mass Transfer **121**, 309–314 (2018).
[51]H. Matin Nikoo, K. Bi, and H. Hao, "Three-dimensional vortex-induced vibration of a circular cylinder at subcritical Reynolds numbers with low-Re correction," Mar. Struct. **66**, 288–306 (2019).
[52]R. Govardhan and C. H. Williamson, "Modes of vortex formation and frequency response of a freely vibrating cylinder," J. Fluid Mech. **420**, 85–130 (2000).
[53]L. Ding, L. Zhang, M. M. Bernitsas, and C. C. Chang, "Numerical simulation and experimental validation for energy harvesting of single-cylinder VIVACE converter with passive turbulence control," Renewable Energy **85**, 1246–1259 (2016).

Vortex-induced vibration of two circular cylinders in a side-by-side arrangement at moderate Reynolds number_ A numerical study

ORIGINALITY REPORT

24%	15%	22%	6%
SIMILARITY INDEX	INTERNET SOURCES	PUBLICATIONS	STUDENT PAPERS

MATCH ALL SOURCES (ONLY SELECTED SOURCE PRINTED)

4%

★ James R. Brown, Margaret D. Madsen, Ayşenur Ateş, Rezawana Islam et al. "Revealing foam stability for cationic and zwitterionic triethylsilyl-containing surfactants", Physics of Fluids, 2023

Publication

Exclude quotes	Off	Exclude matches	Off
Exclude bibliography	On		